



Topology optimization of multi-material active structures to reduce energy consumption and carbon footprint

Wang, Yafeng; Sigmund, Ole

Published in:
Structural and Multidisciplinary Optimization

Link to article, DOI:
[10.1007/s00158-023-03698-3](https://doi.org/10.1007/s00158-023-03698-3)

Publication date:
2024

Document Version
Publisher's PDF, also known as Version of record

[Link back to DTU Orbit](#)

Citation (APA):
Wang, Y., & Sigmund, O. (2024). Topology optimization of multi-material active structures to reduce energy consumption and carbon footprint. *Structural and Multidisciplinary Optimization*, 67(1), Article 5. <https://doi.org/10.1007/s00158-023-03698-3>

General rights

Copyright and moral rights for the publications made accessible in the public portal are retained by the authors and/or other copyright owners and it is a condition of accessing publications that users recognise and abide by the legal requirements associated with these rights.

- Users may download and print one copy of any publication from the public portal for the purpose of private study or research.
- You may not further distribute the material or use it for any profit-making activity or commercial gain
- You may freely distribute the URL identifying the publication in the public portal

If you believe that this document breaches copyright please contact us providing details, and we will remove access to the work immediately and investigate your claim.



Topology optimization of multi-material active structures to reduce energy consumption and carbon footprint

Yafeng Wang¹ · Ole Sigmund¹

Received: 10 July 2023 / Revised: 16 September 2023 / Accepted: 27 October 2023
© The Author(s) 2024

Abstract

A multi-material active structure is a mechanical system made of passive and active materials with the ability to alter its configuration, form, or properties in response to changes in the environment. Active structures have been investigated to design lightweight structures and structures with the ability to “smartly” alter their shapes and/or internal forces. Recently, the potential of active structures to reduce environmental impact, i.e., reduce energy consumption and greenhouse gas (GHG) emissions, has been investigated. It has been verified that, compared to passive structures, active structures can not only use less material but also consume less energy and cause less GHG emissions during their service life, and thus have a significant potential to be applied as environment-friendly mechanical structures. This study aims to develop a general topology optimization (TO) approach to design novel multi-material active structural systems to reduce environmental impact. The approach is based on the density-based TO scheme. Passive and active materials are considered in the TO process and are required to be optimally distributed according to the optimization objective and constraints. The energy consumption or GHG emissions caused by the structure during its service life are treated as the objective function to be minimized under multiple displacement requirements. Typical examples are carried out to verify the developed approach. Results show that the topology optimized active structures may not only achieve significant weight savings but also less energy consumption and GHG emissions compared to equivalent topology optimized passive structures, which indicates that the developed approach has the potential to be applied to design novel structural systems with lighter weight, larger span, and with less environmental impact compared to conventional passive structural systems.

Keywords Multi-material · Topology optimization · Active structure · Energy consumption · Carbon footprint · Greenhouse gas emission

1 Introduction

Substantial progress has been made in structural topology optimization (TO) in the last decades and more and more research and industry fields have employed this versatile technique to realize novel designs with better performance than conventional experience-based designs. Several approaches, such as homogenization (Bendsøe and Kikuchi 1988), solid isotropic material with penalization (SIMP) (Bendsoe and Sigmund 2003), evolutionary structural

optimization (ESO) (Huang and Xie 2010), level set method (Allaire et al. 2004), and geometry projection method (Wein et al. 2020) have been proposed to efficiently carry out the TO on a range of problems.

Since the invention of the structural TO technique, tremendous work and studies have been focused on single-material TO, i.e., the resulting structure is made of only one solid material. In practical engineering applications, it is common to design structures made of multiple materials to achieve lighter-weight or better performances that cannot be realized through a single-material design. For this reason, Thomsen (1992) first proposed a TO approach based on the homogenization technique to maximize the stiffness of a structure consisting of one or two materials. Since then, extensive research on multi-material TO has been carried out by using different methods. Based on the SIMP method, Sigmund and Torquato (1997) and Gibiansky and Sigmund (2000) conducted TO of multi-phase materials with negative thermal expansion

Responsible Editor: Jianbin Du

✉ Yafeng Wang
yafwa@dtu.dk; yafengwang@zju.edu.cn

¹ Department of Civil and Mechanical Engineering, Technical University of Denmark, Koppels Alle 404, 2800 Kongens Lyngby, Denmark

and extremal bulk modulus. Sigmund (2001a) carried out the TO of multi-physics actuators based on a multi-material scheme. Sun and Zhang (2006) studied the microstructure optimization of multiphase materials. Stegmann and Lund (2005) developed a discrete material optimization scheme for composite shell structures. Gao and Zhang (2011) proposed the so-called recursive multiphase materials interpolation (RMMI) and uniform multiphase materials interpolation (UMMI) schemes and compared the effects of mass and volume constraints on the results of multi-material topology. Xu et al. (2021) studied stress-constrained multi-material TO problems by using an ordered SIMP interpolation. Based on an ESO method, Huang et al. (2012) solved multiphase topological optimization problems at multiple scales. Long et al. (2018) introduced a novel concurrent optimization formulation to simultaneously meet the requirements of lightweight design and various constraints. Based on the level set method, Wang and Wang (2004) proposed a ‘color’ level set approach to realize multi-material TO. Liu et al. (2016, 2020) achieved multi-material TO considering the material interface behavior and stress constraint based on the velocity field level set method. Various other methods have also been employed to study specific aspects of multi-material structural TO (Gangl 2020; Chandrasekhar and Suresh 2021; Wang et al. 2022).

In existing studies on stiffness-based multi-material TO, the formulation was often established to minimize the structural compliance subject to a volume or weight constraint for each material phase. However, from a practical point of view, compliance sometimes lacks physical meaning and volume constraints do not make too much sense when the materials have different mass densities. Therefore, minimizing structural weight subject to displacement constraints instead of compliance constraints has significant technical advances in practical engineering design. Compared to compliance minimization studies, the research on multi-material weight minimization is limited. Mirzendehdel and Suresh (2015) treated compliance and weight as the two conflicting objectives to find the best design. Li and Kim (2018) thoroughly investigated multi-material TO weight minimization with a comparison to compliance minimization. Ye et al. (2019) used the independent continuous mapping method to minimize the weight of multi-material structures with a prescribed nodal displacement constraint.

For single-material structures, minimizing structural volume or weight can also be interpreted as minimizing the environmental impact of the structure since less weight usually corresponds to less energy consumption and greenhouse gas (GHG) emissions to produce the material (Xu et al. 2023; You et al. 2023). GHG refers to the gases that contribute to global warming and GHG emissions are often measured in carbon dioxide equivalent (kgCO_2e). For multi-material structures, however, minimizing structural volume or weight does not directly relate to minimizing the environmental impact

because different materials may have different densities, energy intensities, and GHG emission coefficients (Ching and Carstensen 2022). Therefore, to minimize the environmental impact of a multi-material structure through TO, a new objective function encompassing energy consumption or GHG emissions of different materials (i.e., embodied energy or GHG emissions) should be formulated and adopted.

The above-mentioned studies and analyses on multi-material structural TO mostly refer to passive structures (i.e., structures made by multiple passive materials). In recent years, active structures (also known as smart or adaptive structures) have been applied in a wide variety of engineering fields. For example, in the aerospace engineering field, morphing wings have been proposed to actively control their shapes according to practical requirements (Sofla et al. 2010); in the robotics field, active structures have been adopted to design soft robots (Gossweiler et al. 2015); in the civil engineering field, active structures have been employed to control structural vibration (Preumont 2018). Besides, it has been verified that, compared to passive structures, active structures can not only provide configuration-controllability and lightweight features but also have the potential to reduce energy consumption and GHG emissions during their service life (Senatore et al. 2019; Wang and Senatore 2020, 2021; Wang et al. 2021).

Multi-material active structure TO has been investigated by some. For example, Sigmund (2001a, b) proposed a TO method to design multiphysics actuators and electro-thermo-mechanical systems based on material thermal expansion effects through one- and two-material schemes. Wang et al. (2014) conducted a topological design of compliant smart structures embedded with piezoelectric actuators. Jensen et al. (2021) proposed a systematic TO approach for simultaneously designing the morphing functionality and actuation in three-dimensional wing structures in which the actuation was modeled by a thermal-like linear-strain-based expansion in the actuation material. Wang and Sigmund (2023) proposed a decoupled linearized buckling TO framework to maximize the buckling load of multi-material active structures. Existing studies on multi-material active structure TO mainly focus on realizing specific functionality or increasing specific mechanical properties such as shape-morphing capacity or structural stability. However, to our best knowledge, no previous work investigated the environmental impact aspect of multi-material active structures.

As analyzed above, without considering manufacturing procedures, the environmental impact caused by a passive structure mainly depends on the embodied part (i.e., material mass) that corresponds to the production process of the structural material (Cabeza et al. 2021). However, the environmental impact caused by an active structure consists of two parts: the one embodied in the structural material and the operational part related to the actuation control

process (e.g., the energy and GHG emissions caused by the actuation process) (Reksowardojo et al. 2022). Therefore, a new objective function described by the environmental impact consisting of both the two parts (i.e., embodied part and operational part) should be formulated and adopted for the assessment and optimization of multi-material active structures. Note that the manufacturing procedure of multi-material structures, especially considering the interfaces between different materials and joints composed of different materials, may also lead to additional energy consumption. Here we assume that one-time process during the structure’s service life does not contribute significantly to the total energy consumption. If this additional energy consumption needs to be considered, the interfaces between different materials may be identified (Chu et al. 2019; Luo et al. 2019) to assess the energy consumption corresponding to the manufacturing procedure.

This study develops a general TO framework for multi-material active structural systems to minimize the environmental impact. The approach is based on the density-based TO scheme. Passive and active materials are considered in the TO process and are required to be optimally distributed according to the optimization objective and requirements. The environmental impact indicator caused by the structure during its service life is treated as the objective function to be minimized under multiple displacement requirements. By tuning the parameters in the developed mathematical model, the TO framework can be easily modified to realize weight/energy/GHG emissions minimization of a multi-material active structure. Typical examples are carried out to verify the developed approach. Results show that topology-optimized active structures may not only achieve significant weight savings but also less energy consumption and GHG emissions compared to equivalent topology-optimized passive structures.

The outline of the paper is as follows: Sect. 2 introduces a basic introduction and environmental impact assessment of multi-material active structures; Sect. 3 models multi-active material structures in a continuum TO framework and develops the TO model; Sect. 4 presents numerical examples to verify the effectiveness of the proposed approach; finally, Sect. 5 discusses and concludes the paper.

2 Environmental impact assessment of multi-material active structures

2.1 Illustration of a multi-material active structure

Figure 1 illustrates a simple cantilever multi-material active structure composed of a passive and an active material. It is assumed that the deformation of the passive material can only be influenced by external loads while the active

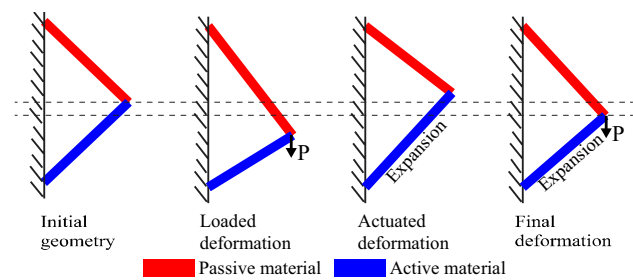


Fig. 1 Illustration for multi-material active structure

material can also change its configuration through active actuation driven by e.g., temperature, pressure, or electromagnetic effects (Qader et al. 2019). The configuration change of the active material will affect the shape and deformation of the entire structure, and thus the structural shape can be actively controlled by strategically enforcing actuation effects.

2.2 Environmental impact assessment

The environmental impact of an active structure is here defined as the energy consumption or GHG emissions caused by the structure during its service life. As analyzed in the Introduction, the environmental impact of an active structure consists of two parts: the part embodied in the structural material and the part related to the actuation control process.

2.2.1 Embodied environmental impact

Assume that an active structure is made of m passive materials and n active materials. The masses are $M_1^{pas}, M_2^{pas}, \dots, M_m^{pas}$ for the passive materials respectively and $M_1^{act}, M_2^{act}, \dots, M_n^{act}$ for the active materials respectively, in which the superscript “*pas*” and “*act*” refer to passive and active respectively. The environmental impact coefficients are $\alpha_1^{pas}, \alpha_2^{pas}, \dots, \alpha_m^{pas}$ for the passive materials and $\alpha_1^{act}, \alpha_2^{act}, \dots, \alpha_n^{act}$ for the active materials, respectively. Then, the simplified embodied environmental impact I_{emb} of the active structure without considering manufacturing cost is given by

$$I_{emb} = \sum_{i=1}^m M_i^{pas} \alpha_i^{pas} + \sum_{i=1}^n M_i^{act} \alpha_i^{act} \tag{1}$$

In practical design, if the energy consumption is to be minimized, the environmental impact coefficients can be chosen as material energy intensity (unit: energy per unit mass) while if the carbon footprint is to be minimized, the

environmental impact coefficients can be chosen as material GHG emission intensity (unit: GHG emissions per unit mass).

2.2.2 Operational environmental impact

A mechanical structure will usually undergo external loadings multiple times during its service life. For an active structure, actuation may or may not be needed each time an external load is applied. If actuation is needed to control the configuration of a loaded structure, operational energy is required. Without loss of generality, assume that the active structure will undergo k external loadings during its service life and the operational energy cost for the actuation of each material is E_i^j ($i = 1, 2, \dots, n$ and $j = 1, 2, \dots, k$). The environmental impact coefficients are $\beta_1^{\text{act}}, \beta_2^{\text{act}}, \dots, \beta_n^{\text{act}}$ for the energy consumption of active materials. Then the operational environmental impact I_{opt} of the active structure is given by

$$I_{\text{opt}} = \sum_{i=1}^n \sum_{j=1}^k E_i^j \beta_i^{\text{act}} \tag{2}$$

In practical design, if energy consumption is considered to be minimized, the environmental impact coefficient is set to 1.0, while if the GHG emission is considered to be minimized, the environmental impact coefficient is set as the GHG emission intensity for the source energy consumption (unit: GHG emissions per unit energy).

2.2.3 Total environmental impact

Based on Eqs. (1) and (2), the total environmental impact of the multi-material active structure is computed by

$$I = I_{\text{emb}} + I_{\text{opt}} \tag{3}$$

3 Multi-material active structure modeling and topology optimization

3.1 Active structure modeling

In this study, two-material active structures under one or two load cases are considered but the concept is general and may be applied to more than two materials and more than two load cases. Following the method proposed in Sigmund (2001a), it is assumed that the passive material has a zero while the active material has a non-zero thermal expansion coefficient and thus the active material can be driven actively by temperature variation. Thermal expansion is used as a strategy here to simulate various

linear-strain-based actuation effects such as shape memory alloys (SMA) and piezoelectric (PZT) materials.

In existing studies on TO of multi-material active structures (Sigmund 2001a; Jensen et al. 2021), two design variables per element, i.e., a material density design variable and a material phase design variable, are introduced for a regular finite element mesh to parameterize the material distribution. This strategy is only applicable for single-load cases because active material can only have one actuation effect (expansion or contraction) for the considered load case. For two load cases, the active material may need to have different actuation effects.

To account for two load cases, the material modeling method is extended to define three design variables, ξ_e , η_e , and χ_e ($\in [0, 1]$), per element to parameterize not only the material distribution but also the actuation effects of the element. ξ_e is used to determine the material relative density (solid or void) field, η_e is used to determine the material phase (passive or active), and χ_e is used to determine the actuation effect (expansion or contraction) of the element. Based on the material model, $\xi_e = 0$ indicates that the element is occupied by void; $\xi_e = 1$ and $\eta_e = 0$ indicate that the element is occupied by passive material; $\xi_e = 1$, $\eta_e = 1$, and $\chi_e = 0$ indicate that the element is occupied by active material with contraction effect while $\xi_e = 1$, $\eta_e = 1$, and $\chi_e = 1$ indicate that the element is occupied by active material with expansion effect. The material model following the above-mentioned strategy is illustrated in Fig. 2.

3.2 Topology optimization model

3.2.1 Design variables, filtering, and projections

Following the proposed material model, the design variable vector can be expressed as

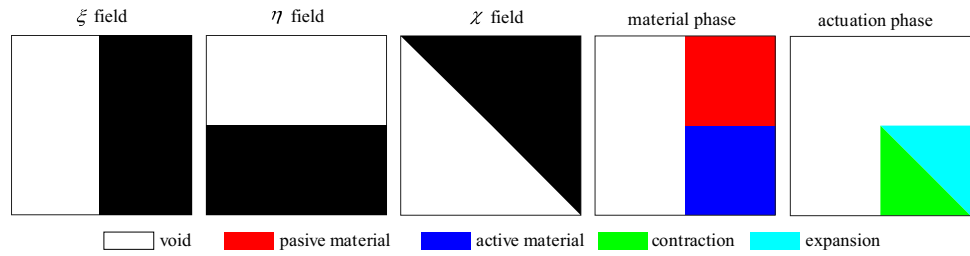
$$\mathbf{x} = \{\boldsymbol{\xi}, \boldsymbol{\eta}, \boldsymbol{\chi}\}^T \tag{4}$$

where $\boldsymbol{\xi} = \{\xi_e\}$, $\boldsymbol{\eta} = \{\eta_e\}$, and $\boldsymbol{\chi} = \{\chi_e\}$. To avoid mesh dependency and checkerboard patterns (Bendsoe and Sigmund 2003) and enhance the discreteness of the designs, a three-field approach (Wang et al. 2011) is employed. Take design variable ξ_e as an example, the elementwise density field are first filtered by using the density filter

$$\bar{\xi}_e = \frac{1}{\sum_{i \in N_e} H_{ei}} \sum_{i \in N_e} H_{ei} \xi_i \tag{5}$$

where $\bar{\xi}_e$ is the filtered design variables, N_e is the set of elements i for which the center-to-center distance $\Delta(e, i)$ to element e is smaller than the filter radius r_{min} , and is the typical linear distance function

Fig. 2 Material model for two-material active structure under two load cases



$$H_{ei} = \max(0, r_{\min} - \Delta(e, i)) \tag{6}$$

Physical density fields are then obtained by a modified smooth Heaviside function

$$\tilde{\xi}_e = \frac{\tanh(\mu\theta) + \tanh\left(\mu\left(\frac{\tilde{\xi}_e}{\xi_e} - \theta\right)\right)}{\tanh(\mu\theta) + \tanh(\mu(1 - \theta))} \tag{7}$$

where μ controls the steepness/sharpness of the function and θ sets the threshold value. Filtered and physical fields for design variables η_e and χ_e can be calculated similarly.

The design-dependent stiffness matrix \mathbf{K} is assembled from the element ones, i.e., $\mathbf{k}_e(\tilde{\xi}_e, \tilde{\eta}_e)$, which is parameterized by interpolation functions as

$$\mathbf{k}_e(\tilde{\xi}_e, \tilde{\eta}_e) = h(\tilde{\xi}_e, \tilde{\eta}_e)\mathbf{k}_0 \tag{8}$$

where local finite element matrix \mathbf{k}_0 corresponds to unit elastic modulus and is independent of $\tilde{\xi}_e$ and $\tilde{\eta}_e$. Note that the global stiffness matrix \mathbf{K} is independent of variable $\tilde{\chi}_e$ because it only controls the thermal loading effect through temperature variation ΔT_e , i.e., only affects the right-hand side of the FE equilibrium equation.

The three-phase material model proposed by Sigmund (2001a) to interpolate the elemental material properties (shear modulus G , bulk module K , and thermal expansion coefficient α) is employed, given as

$$\begin{aligned} G(\tilde{\xi}_e, \tilde{\eta}_e) &= \tilde{\xi}_e^p \Phi_G(\tilde{\eta}_e) \\ K(\tilde{\xi}_e, \tilde{\eta}_e) &= \tilde{\xi}_e^p \Phi_K(\tilde{\eta}_e) \\ \alpha(\tilde{\eta}_e) &= \frac{(K_1\alpha_1 - K_2\alpha_2)K(\tilde{\eta}_e) - K_1K_2(\alpha_1 - \alpha_2)}{K(\tilde{\eta}_e)(K_1 - K_2)} \end{aligned} \tag{9}$$

where K_1 and K_2 are respectively the bulk moduli of materials 1 and 2, α_1 and α_2 are respectively the thermal expansion coefficients of materials 1 and 2, and the phase interpolation $\Phi_G(\tilde{\eta}_e)$ and $\Phi_K(\tilde{\eta}_e)$ are defined as

$$\begin{aligned} \Phi_G(\tilde{\eta}_e) &= (1 - \Psi)G_L^{\text{HSW}}(\tilde{\eta}_e) + \Psi G_U^{\text{HSW}}(\tilde{\eta}_e) \\ \Phi_K(\tilde{\eta}_e) &= (1 - \Psi)K_L^{\text{HS}}(\tilde{\eta}_e) + \Psi K_U^{\text{HS}}(\tilde{\eta}_e) \end{aligned} \tag{10}$$

In the above formulations, G_L^{HSW} and G_U^{HSW} are the lower and upper Hashin–Shtrikman–Walpole (HSW) bounds on

the shear modulus, and K_L^{HS} and K_U^{HS} are the lower and upper Hashin–Shtrikman (HS) bounds on the bulk modulus. Their exact formulas depend on the property values (shear and bulk modulus) of the two materials (for more details about the exact formulas the reader is referred to Sigmund (2001a)). $\Psi \in [0, 1]$ interpolates linearly between the lower and upper bounds and works as a penalization mechanism for intermediate densities, and $\Psi = 1$ is adopted in this study. $K(\tilde{\eta}_e)$ is found from Eq. (9) by setting $\tilde{\xi}_e = 1$. Note that by using the three-phase material interpolation functions, all the physical parameters can be ensured to be within the physically realizable bounds for any densities (Sigmund 2001a).

For two-dimensional plane stress problems, the interpolation for Young’s modulus is expressed as

$$h(\tilde{\xi}_e, \tilde{\eta}_e) = \frac{4K(\tilde{\xi}_e, \tilde{\eta}_e)G(\tilde{\xi}_e, \tilde{\eta}_e)}{K(\tilde{\xi}_e, \tilde{\eta}_e) + G(\tilde{\xi}_e, \tilde{\eta}_e)} \tag{11}$$

3.2.2 Governing equations

The FE equilibrium equation of a structure under thermo-mechanical loading can be described as

$$\mathbf{K}\mathbf{U} = \mathbf{P} \tag{12}$$

where \mathbf{P} is the load vector consisting of mechanical load \mathbf{P}_m and thermal load \mathbf{P}_t , i.e., $\mathbf{P} = \mathbf{P}_m + \mathbf{P}_t$, and \mathbf{U} is the nodal displacement vector. Based on a linear analysis assumption, Eq. (12) can be decoupled as

$$\begin{cases} \mathbf{K}\mathbf{U}_m = \mathbf{P}_m \\ \mathbf{K}\mathbf{U}_t = \mathbf{P}_t \end{cases} \tag{13}$$

where \mathbf{U}_m and \mathbf{U}_t are the nodal displacement vectors caused by mechanical load and thermal load respectively. Note that, \mathbf{U}_m , \mathbf{U}_t , and \mathbf{U} satisfy $\mathbf{U}_m + \mathbf{U}_t = \mathbf{U}$.

For a regular discrete finite element model, the thermal load vector \mathbf{P}_t is given by

$$\mathbf{P}_t = \sum_e \int_{V_e} \mathbf{B}_e^T \mathbf{D}_e \boldsymbol{\varepsilon}_{t,e} dV \tag{14}$$

where $\mathbf{B}_e, \mathbf{D}_e, \boldsymbol{\varepsilon}_{t,e}$, and V_e are respectively the strain–displacement matrix, constitutive matrix, thermal strain, and volume of element e . Thermal strain $\boldsymbol{\varepsilon}_{t,e}$ is given by

$$\boldsymbol{\varepsilon}_{t,e} = \alpha_e \boldsymbol{\Phi}^T \Delta T_e \tag{15}$$

where α_e and ΔT_e are respectively the thermal expansion coefficient and temperature variation of element e , and $\boldsymbol{\Phi} = [1 \ 1 \ 0]^T$ is a constant vector for two-dimensional problems. ΔT_e is determined by the design variable χ_e by

$$\Delta T_e = (2\bar{\chi}_e - 1)\Delta T_0 \tag{16}$$

where ΔT_0 is a user-defined constant reference temperature variation.

3.2.3 Displacement constraints

From a practical point of view, displacement constraints, instead of compliance constraints, have more significant technical implications for structural design. Requiring that the displacement u_i for the i th ($i \in \Theta$) degree of freedom (DOF) is within the upper bound \bar{u}_i and lower bound \underline{u}_i , i.e., $u_i \in [\underline{u}_i, \bar{u}_i]$, where Θ denotes the index set of the DOFs with displacement limits, then the displacement constraints can be expressed as

$$\underline{u}_i \leq u_i \leq \bar{u}_i, \quad i \in \Theta \tag{17}$$

Without loss of generality, assume that $\underline{u}_i < 0$ and $\bar{u}_i > 0$ ($\forall i \in \Theta$), then Eq. (17) can be transformed into two inequalities as

$$\begin{cases} u_i/\underline{u}_i - 1 \leq 0 \\ u_i/\bar{u}_i - 1 \leq 0 \end{cases}, \quad i \in \Theta \tag{18}$$

If a large number of DOFs need to be displacement-limited, a lot of local constraints as expressed in Eq. (18) have to be considered in the optimization, which may affect the computational efficiency. To alleviate this issue, the local constraints Eq. (18) can be transformed into two global constraints as

$$\begin{cases} \max(u_i/\underline{u}_i) - 1 \leq 0 \\ \max(u_i/\bar{u}_i) - 1 \leq 0 \end{cases}, \quad i \in \Theta \tag{19}$$

Based on the Kreisselmeier–Steinhauser (K–S) aggregation function (Kreisselmeier and Steinhauser 1980), the maximum values in Eq. (19) can be approximated as

$$\begin{cases} \max(u_i/\underline{u}_i) \approx J^{\text{KS}}(u_i/\underline{u}_i) \\ \max(u_i/\bar{u}_i) \approx J^{\text{KS}}(u_i/\bar{u}_i) \end{cases} \tag{20}$$

where $J^{\text{KS}}(u_i/\underline{u}_i)$ and $J^{\text{KS}}(u_i/\bar{u}_i)$ are given by

$$\begin{cases} J^{\text{KS}}(u_i/\underline{u}_i) = u_i/\underline{u}_i + \frac{1}{q} \ln \left(\sum_{i \in \Theta} e^{q(u_i/\underline{u}_i - u_i/\underline{u}_i)} \right) \\ J^{\text{KS}}(u_i/\bar{u}_i) = u_i/\bar{u}_i + \frac{1}{q} \ln \left(\sum_{i \in \Theta} e^{q(u_i/\bar{u}_i - u_i/\bar{u}_i)} \right) \end{cases} \tag{21}$$

where q is the aggregation parameter.

The K–S aggregation function is only an approximation of the maximum value which may deviate from the exact value during the optimization process. For a better approximation, a normalization strategy similar to that proposed for maximum stress approximations (Le et al. 2010; De Leon et al. 2015) is adopted in this study. Take the approximation $J^{\text{KS}}(u_i/\underline{u}_i)$ as an example, it is normalized by a parameter c in the optimization, i.e.,

$$\tilde{J}^{\text{KS}}(u_i/\underline{u}_i) = c J^{\text{KS}}(u_i/\underline{u}_i) \tag{22}$$

The normalization parameter c is updated as follows during the optimization

$$c^n = \kappa^n \frac{[\max(u_i/\underline{u}_i)]^{n-1}}{[\tilde{J}^{\text{KS}}(u_i/\underline{u}_i)]^{n-1}} + (1 - \kappa^n)c^{n-1} \tag{23}$$

where n is the optimization iteration number and κ is a parameter that controls the update of c between iterations. In this work, $\kappa^n = 0.5$ for all n and $c^0 = 1$ are adopted. Similarly, normalization $\tilde{J}^{\text{KS}}(u_i/\bar{u}_i)$ can be defined for $J^{\text{KS}}(u_i/\bar{u}_i)$. Then the global displacement Eq. (19) is re-expressed as

$$\begin{cases} \tilde{J}^{\text{KS}}(u_i/\underline{u}_i) - 1 \leq 0 \\ \tilde{J}^{\text{KS}}(u_i/\bar{u}_i) - 1 \leq 0 \end{cases} \tag{24}$$

Note that c^n is not considered in the sensitivity analysis. In general, c^n converges quickly and we experience no convergence problems despite changing the coefficient every iteration.

3.2.4 Objective function

Following the analysis in Sect. 2, the total environmental impact (energy consumption or GHG emissions) is adopted as the objective function to be minimized.

3.2.4.1 Embodied energy calculation Based on the proposed material model and the design variables defined above, the masses of the two materials can be computed by

$$M_{act} = \rho_{act} \sum_e V_e \tilde{\xi}_e \tilde{\eta}_e, \quad M_{pas} = \rho_{pas} \sum_e V_e \tilde{\xi}_e (1 - \tilde{\eta}_e) \tag{25}$$

where ρ_{act} and ρ_{pas} are the mass densities of the active and passive materials respectively. Then, the embodied environmental impact of the active structure is given by

$$I_{emb} = \alpha_{act}M_{act} + \alpha_{pas}M_{pas} \tag{26}$$

where α_{act} and α_{pas} are the environmental impact coefficients of active and passive materials respectively.

3.2.4.2 Operational energy calculation For the operational part, it is necessary to first compute the energy consumption for the actuation. Two different assumptions can be adopted to compute the operational energy for an active structure:

- (1) assuming that the external loading is first applied and then followed by the actuation; and
- (2) assuming that the external and actuation loadings are applied simultaneously.

Assuming linear analysis and linear elastic materials, the structural end states (e.g., internal stress and strain) obtained by the two ways are identical, but the value of the operational energy consumed for actuation may be different.

A simple example shown in Fig. 3 is used to illustrate the difference between the two assumptions on the computation of operational energy. The horizontal bar with a constant cross-sectional area A is composed of two elements of the same size: the left one is made of active material and the right one is made of passive material. Assume that the two materials have the same Young's modules E and zero Poisson's ratios.

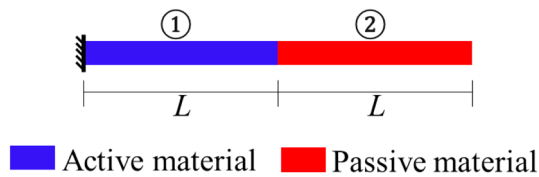
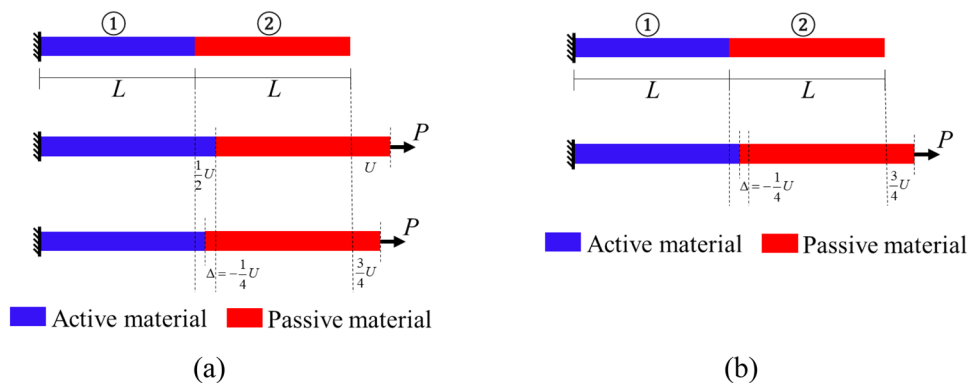


Fig. 3 Illustrative example for computation of operational energy

Fig. 4 Illustrations for different operational energy computation methods: a assumption #1 and b assumption #2



(1) Operational energy consumption based on assumption #1.

Figure 4a is used to illustrate the operational energy computation based on the first assumption. Assume that a horizontal external load P is firstly applied at the end of the bar, which causes a total elongation of U , and both the two elements have a deformation of $U/2$ at their ends (middle in Fig. 4a). Solving the equilibrium equation results in $U = \frac{2PL}{EA}$. Then, an actuation elongation of $\Delta = -\frac{1}{4}U$ is enforced on element ① such that the total displacement of the bar reduces to $\frac{3}{4}U$ (bottom in Fig. 4a).

Since the loading process is assumed to be a quasi-static process, the force equilibrium condition is always satisfied, which means that the horizontal internal force of the two elements is equal to P during the actuation process. Therefore, the operational energy consumed by element ① during the actuation under actuation elongation of Δ can be calculated by

$$E_{operational}^{①} = P \cdot \frac{1}{4}U = \frac{P^2L}{2EA} \tag{27}$$

Element ② is passive hence $E_{operational}^{②} = 0$. Therefore, the total operational energy is

$$E_{operational} = E_{operational}^{①} + E_{operational}^{②} = \frac{P^2L}{2EA} \tag{28}$$

(2) Operational energy consumption based on assumption #2.

Figure 4b is used to illustrate the operational energy computation based on the second assumption. Since the actuation is applied simultaneously with the external loading, the operational energy consumed by element ① during the actuation under actuation elongation of Δ is given by

$$E_{operational}^{①} = \frac{1}{2} \cdot P \cdot \frac{1}{4}U = \frac{1}{8}PU = \frac{P^2L}{4EA} \tag{29}$$

$E_{operational}^{②} = 0$ still holds. Therefore, the total operational energy is

$$E_{\text{operational}} = E_{\text{operational}}^{(1)} + E_{\text{operational}}^{(2)} = \frac{P^2 L}{4EA} \quad (30)$$

Comparing the results obtained by following the two assumptions it can be seen that $E_{\text{operational}}$ computed by assumption #1 is larger than that obtained by assumption #2. In this study, assumption #1 is adopted to consider an upper bound of $E_{\text{operational}}$ in the design, which is conservative to account for the contribution of operational energy.

Notably, the operational energy cost by the actuation is not guaranteed to be always positive. When an actuation length extension is enforced for an active element under tension or vice versa for the element under compression, the resulting operational energy will be negative. Again, take the bar as an example, Fig. 5 shows a situation that element ① has an actuation elongation of $\Delta = \frac{1}{4}U$, then following the same analysis procedure as above, the resulting operational energy is $E_{\text{operational}} = -\frac{P^2 L}{2EA}$. In such cases, no work is needed because there is an actual gain of energy that may be harvested. During TO, if energy harvesting is not intended to be considered, which is the focus of this study, the energy gain value of certain elements can be set to zero. This treatment will make the operational energy functions of the corresponding elements non-differentiable at zero value, but numerical tests show that this does not affect the convergence stability of the optimization. If energy harvesting needs to be considered, the formulation has the potential to be applied for optimizing active material distribution for better energy harvesting capacity.

For a general active continuum structure, following assumption #1, $E_{\text{operational}}$ can be calculated by

$$E_{\text{operational}} = -\left(\int_V (\boldsymbol{\sigma}_m)^T \boldsymbol{\varepsilon}_t dV + \frac{1}{2} \int_V (\boldsymbol{\sigma}_t)^T \boldsymbol{\varepsilon}_{\Delta T} dV \right) \quad (31)$$

where $\boldsymbol{\sigma}_m$ and $\boldsymbol{\sigma}_t$ are the stresses caused by mechanical loading and thermal loading respectively that are given by

$$\boldsymbol{\sigma}_m = \mathbf{D}\mathbf{B}\mathbf{U}_m, \quad \boldsymbol{\sigma}_t = \mathbf{D}(\mathbf{B}\mathbf{U}_t - \boldsymbol{\varepsilon}_t) \quad (32)$$

Substituting Eq. (32) into Eq. (31) gives

$$E_{\text{operational}} = -\left(\int_V (\mathbf{U}_m)^T \mathbf{D}\mathbf{B}^T \boldsymbol{\varepsilon}_t dV + \frac{1}{2} \int_V (\mathbf{U}_t)^T \mathbf{D}\mathbf{B}^T \boldsymbol{\varepsilon}_t dV - \frac{1}{2} \int_V (\boldsymbol{\varepsilon}_{\Delta T})^T \mathbf{D}\boldsymbol{\varepsilon}_t dV \right) \quad (33)$$

Considering that $\mathbf{P}_t = \int_V \mathbf{D}\mathbf{B}^T \boldsymbol{\varepsilon}_t dV$, Eq. (33) can be simplified as

$$E_{\text{operational}} = -\left(\mathbf{U}_m + \frac{1}{2}\mathbf{U}_t \right)^T \mathbf{P}_t + \frac{1}{2} \int_V (\boldsymbol{\varepsilon}_t)^T \mathbf{D}\boldsymbol{\varepsilon}_t dV \quad (34)$$

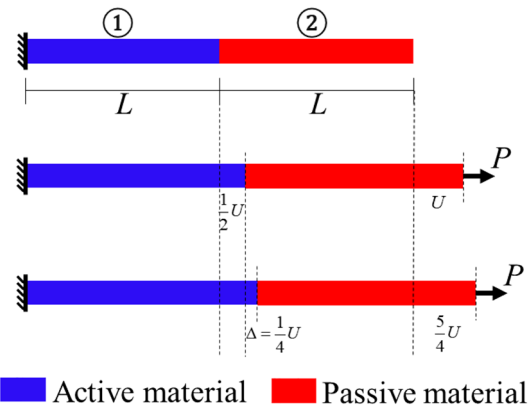


Fig. 5 Illustration for the case of negative operational energy

Note that instead of the method above, the operational energy can also be computed from a global energy conversion point of view, which is explained in Appendix 1.

With the operational energy for each load case obtained, the operational environmental impact of the active structure can be computed as

$$I_{\text{opt}} = \lambda\beta \sum_j g^j E_{\text{operational}}^j \quad (35)$$

where β is the environmental impact coefficient for the source energy, λ is energy transformation efficiency, $E_{\text{operational}}^j$ is the operational energy cost under the j^{th} load case, and g^j is the number of times that the j^{th} load case is applied during the service life of the structure.

3.2.4.3 Final weighted objective function Based on I_{emb} and I_{opt} , the final weighted objective function is defined as

$$f = wI_{\text{emb}} + (1 - w)I_{\text{opt}}, \quad w \in [0, 1] \quad (36)$$

where w is a parameter to control the optimization target. By tuning the values of w in the objective function, different optimization targets can be realized. For example, when $w = 1/2$, the resulting objective function can be used to minimize the total environmental impact; when $w = 1$, the resulting objective function can be used to only minimize the embodied environmental impact. Together with tuning the values of α_{act} and α_{pas} , i.e., $\alpha_{\text{act}} = \alpha_{\text{pas}} = w = 1$, the resulting objective function can be used to minimize only the weight of the structure.

3.3 Sensitivity analysis

The adjoint method (Bendsoe and Sigmund 2003) is employed to calculate the sensitivities of the objective and constraint functions with respect to the physical-field variables (see details in Appendix 2), then the sensitivities with

respect to the design variables are calculated by using the chain rule.

4 Numerical examples

In this Section, three numerical examples are studied to verify the proposed approach. In the finite element analysis, four-node bilinear elements are used, and plain stress assumption is adopted. In the optimization, the parameter in the K–S function is set to $q = 100$ and the projection parameter is set to $\theta = 0.5$. A continuation approach is employed for the projection parameter μ which starts with $\mu = 2$ and then is raised by $\Delta\mu = 2$ each 25 optimization steps from the 200th iteration, up to the value $\mu = 32$. The method of moving asymptotes (MMA) (Svanberg 1987) with an external move limit of 0.1 is adopted to solve all the optimization problems. The stop criterion for the optimizations is that the relative change of the maximum absolute value of design variables of two consecutive iterations is smaller than the tolerance of 0.001% or the iteration number reaches a limit of 600.

In the following examples, the materials given in Table 1 are employed. The GHG intensity of electricity used for actuation is taken as $\beta = 0.16$ (unit: $\text{kgCO}_2\text{e}/\text{MJ}$) and the electricity utilization efficiency is $\lambda = 0.5$. The

reference temperature variation for the actuation is set to $|\Delta T_0| = 50\text{ }^\circ\text{C}$. Note that, the actuation effects of active material can either be expansion or contraction depending on the design variable χ .

Notably, considering the uneven industrial development levels in different countries and regions, the same material produced in different places or countries may have different GHG intensity and embodied energy intensity coefficients, which will affect the weights to be chosen for different materials in the optimization. The proposed approach is a general framework for active structures made of multiple materials, and specific parameters of materials can be determined according to the production regions and design requirements in a practical design.

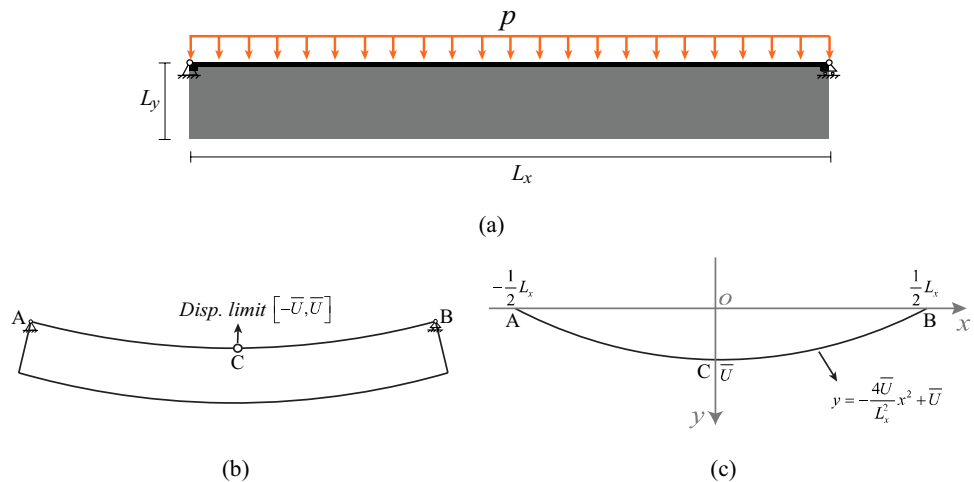
4.1 Simply-supported bridge structure

In this example, a simply-supported bridge structure as shown in Fig. 6a is considered to demonstrate the effectiveness of the proposed approach for single-load case situations. The sizes are $L_x = 10\text{ m}$ and $L_y = 1\text{ m}$. An evenly distributed loading of $p = 0.5\text{ kN/m}$ is applied at the top of the structure. The service life of the structure is assumed to be 30 years and the average frequency of application of loading is 5 times per hour. Displacement limits are applied to all the vertical DOFs of the top nodes. To ensure a smooth deformation of the top surface, different displacement limits

Table 1 Properties of passive and active material

Type	Material no.	Density (g/cm^3)	Young’s modulus (GPa)	Embodied energy intensity (MJ/kg)	GHG intensity ($\text{kgCO}_2\text{e}/\text{kg}$)	Thermal expansion ($^\circ\text{C}$)
Passive material	1	2.70	70	120	13	0
Active material	2	7.10	80	95	8	2×10^{-5}

Fig. 6 Design domain and displacement limits of simply-supported bridge structure: **a** design domain and loading, **b** deformation shape under evenly distributed loading, and **c** displacement limits set for the upper surface



are defined for different DOFs. Under an evenly-distributed loading, the approximately deformed shape of the structure is shown in Fig. 6b. The deformed shape of the top line is close to a quadratic curve, therefore, the values defined by a quadratic curve as shown in Fig. 6c are taken as the displacement limits for the corresponding DOFs of the nodes on the top. Note that the displacement limit for the vertical DOF at the midpoint C is set to $[-\bar{U}, \bar{U}]$ where $\bar{U} = \frac{1}{500}L_x$.

The design domain is discretized into 600×60 square elements and a filter radius of $r_{\min} = 7.5$ is adopted in the optimization. Two square domains with a size of 6×6 elements at the two supports are set as passive domains that are occupied by passive material and a small rectangular area with a width of three elements on the top of the design domain is set as the passive domain that should be occupied by solid material. The distributed loading is applied to all the top nodes of the structure.

4.1.1 Weight minimization

Firstly, weight minimization is carried out for the two-material active bridge structure. Since the weight of the structure only depends on the masses of the two materials, the environmental impact coefficient and the operational part are not considered in the objective function. For comparison, weight minimization is also carried out for the corresponding passive structure without considering the actuation effect of active material.

Figure 7a and b shows the optimized designs of the weight-minimized active and passive structures, respectively. As can be seen, the active structure is made of two materials while the passive structure is made of only passive material. This is because actuation is not considered in passive structure hence the optimizer chooses the more stiffness-efficient material to passively resist the loading. In contrast, actuation is considered for the active structure, which makes it more advantageous to use some active material for actively reducing the deformation. On the other hand, the active material has a larger density than the passive material, hence it may not be the best choice to use all active material for the structure. In the optimization, the optimizer chooses the two materials and their layouts automatically and resulting in a design made of 3.20 kg active material and 4.44 kg passive material. Compared

to the passive design, the active design has much smaller structural component sizes, which results in a 28.20% reduction of the structural weight.

The passive and active designs have different topologies and the main difference is that two more members are generated on the sides in the active structure. The main function of the two members is to support the two horizontal thin members on the sides to reduce their deformation because the top surface on the two sides of the structure has relatively smaller displacement limits according to that defined in Fig. 6c. Because the passive structure has larger member sizes, which can ensure the satisfaction of all the displacement limits, the two members are not necessary. Figure 8a and b shows the final deformations of the two structures. Both structures exhibit smooth deformations on their top surfaces as defined in Fig. 6c. For comparison, Fig. 8c and d shows the designs with all the top nodes enforced with the same displacement limit of $[-\bar{U}, \bar{U}]$. The two optimized designs achieve slightly smaller weights, however, the deformation of the top surface is not smooth, especially at the two ends, even though all the displacement limits are respected. From a practical point of view, enforcing different displacement limits for different nodes could be helpful and preferable to ensure a smooth structural deformation.

The actuation of active material also contributes to the reduction of deformation. Figure 9 shows the actuation effects of the active material in the active structure. As can be seen, active materials in different positions have different effects: the active material distributed at the top chord expands while the active material distributed at the bottom chord contracts. The two actuation effects lead to upward deformation of the structure, which is used to counteract the deformation caused by the external downward load. In addition, both the active material in the top and bottom chords are mainly distributed in the middle, which can maximize the actuation effects. Figure 10 shows the structural deformations caused by the external loading and actuation, the union of which are the final deformation of the structure.

This example shows that the optimized active structure can achieve a significant weight saving compared to the corresponding optimized passive structure. However, weight reduction is at the cost of the energy used for actuation; whether active designs could outperform passive

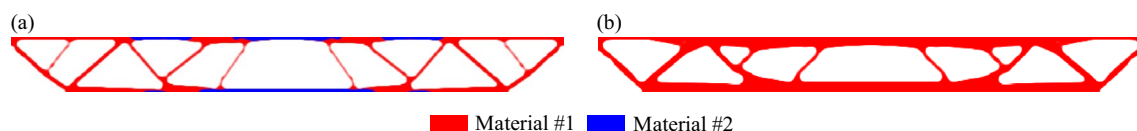


Fig. 7 Optimized designs for weight minimization: **a** optimized active structure and **b** optimized passive structure

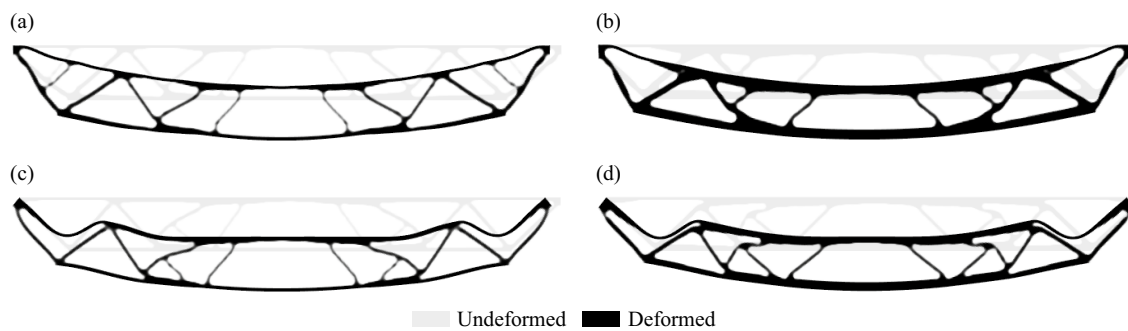


Fig. 8 Deformations under smooth and non-smooth displacement limits: **a** and **c** are respectively deformations of active structure under smooth and non-smooth displacement limits; **b** and **d** are respectively

deformations of passive structure under smooth and non-smooth displacement limits

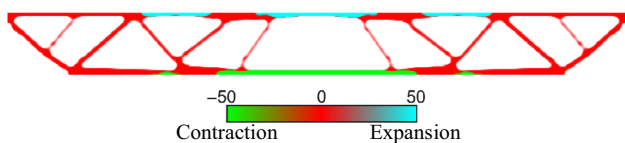


Fig. 9 Actuation effects of active material

designs regarding energy consumption is investigated in the following examples.

4.1.2 Energy minimization

The total energy consumption of an active structure consists of two parts: embodied and operational. Embodied energy minimization and total energy minimization are respectively

carried out in the following to design active structures. For comparison, energy minimization is also carried out for the corresponding passive structure that does not consider the actuation effect of the active material. Note that the energy consumption of a passive structure only comes from the embodied part.

Figure 11a and b show the optimized designs for the embodied energy minimization of active and passive structures, respectively. Similar to the weight-minimized designs, the active structure is made of the two materials defined in Table 1 while the passive structure is made of only passive material. The distribution of the two materials in the active structure is similar to that obtained by weight minimization but the material amounts are slightly different. The embodied energies corresponding to the two materials are 427.02 MJ and 369.29 MJ, respectively. The

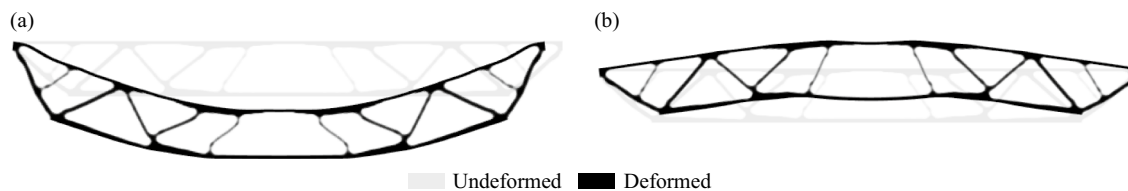


Fig. 10 Deformations caused by **a** external loading and **b** actuation

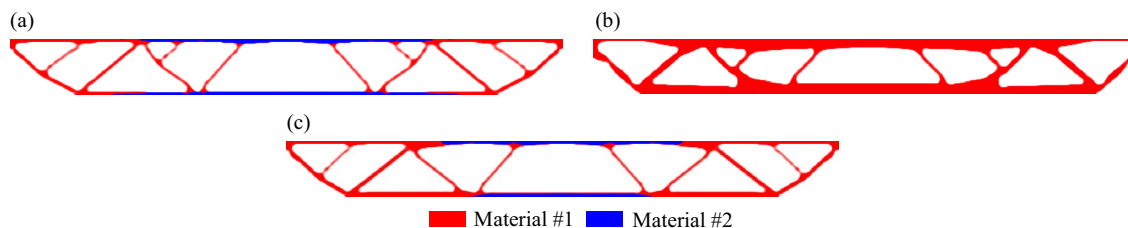


Fig. 11 Optimized designs for energy minimization: **a** embodied energy-minimized active structure, **b** energy-minimized passive structure, and **c** total energy-minimized active structure

comparison indicates that the active design has 39.43% less embodied energy consumption than the passive design, which implies that the active solution outperforms the passive solution regarding embodied energy consumption. In fact, embodied energy minimization is similar to weight minimization for an active structure because they both do not consider the operational part caused by the actuation. The operational energy cost by the actuation of the active structure is 167.46 MJ, which leads to a total energy consumption of 963.77 MJ. However, since the operational energy was not considered in the objective function, the active structure may not be a better solution in terms of total energy consumption.

Figure 11c shows the optimized design of the active structure through total energy minimization, i.e., both the embodied and operational energies are considered in the objective function. The obtained structure also consists of two materials, but the amount of active material is less than that in the active structure obtained through embodied energy minimization. This is because too much active material will lead to a higher operational energy consumption that will significantly increase the total energy consumption. Also, two short inclined components supporting the top chord disappear because the increased component size of the top chord can provide sufficient stiffness. The embodied and operational energy consumptions of the total energy-minimized active structure are 837.36 MJ and 115.22 MJ respectively, which leads to a lower total energy consumption of 952.58 MJ compared to the active and passive structures obtained through embodied energy minimization. This result indicates that total energy minimization is a more appropriate strategy for active structures to reduce energy consumption.

Figure 12a and b show the actuation effects of the active materials in the two optimized active structures. As can be seen, the actuation effects are similar to that in the weight-minimized design. The active material distributed at the top chord expands while the active material distributed at

the bottom chord contracts. The two actuation effects lead to upward deformation of the structure, which is used to counteract the deformation caused by the external downward load. Fig. 12c and d show the final deformation of the two structures with all the nodal displacements within the limits.

This example shows that optimized active designs can achieve energy saving compared to the corresponding passive design. Carbon footprint is another measure of a structure on the environmental impact; the GHG emission minimization of active structures is investigated in the following example.

4.1.3 GHG emission minimization

By replacing the energy intensity coefficients with GHG emission intensity coefficients in the objective function, GHG emission minimization can be carried out. Similar to energy minimization, embodied GHG emission minimization and total GHG emission minimization are respectively conducted for active structures and benchmarked with the corresponding optimized passive designs.

Figure 13a and b show the optimized designs for active structures obtained through embodied GHG emission minimization and total GHG emission minimization, respectively. Similar to energy minimization, the active structure obtained through total GHG emission minimization has less active material than that obtained through embodied GHG emission minimization. Though the active structure obtained through total GHG emission minimization has a larger embodied GHG emission of 82.37 kgCO₂e than 74.51 kgCO₂e obtained by embodied GHG minimization, it achieves a smaller total GHG emission of 101.55 kgCO₂e. Also, the passive design (Fig. 13c) has a GHG emission of 140.01 kgCO₂e, which is larger than the two optimized active structures. This result indicates that the active design obtained through GHG emission minimization could achieve less GHG emissions compared to the corresponding passive design.

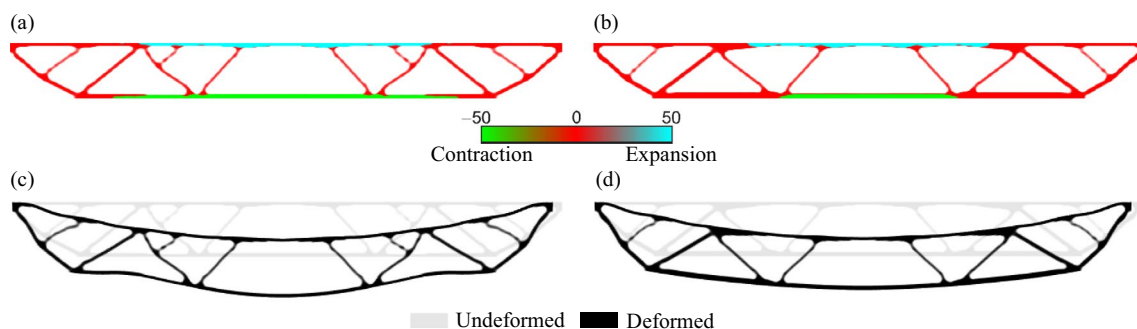


Fig. 12 Actuation effects of active material in optimized active structures and the corresponding deformations: **a** and **b** are respectively optimized designs for embodied and total energy minimization; **c** and **d** are respectively final deformations of the two structures

The active material distributions and actuation effects (Fig. 14) are similar to the designs obtained through weight and energy minimization but with slightly more active material since the GHG coefficient ratio is smaller than the energy coefficient ratio. With the help of actuation, all the displacement limits are respected in the final deformation of the structure.

4.2 Cantilever structure

In this example, a cantilever structure as shown in Fig. 15 is considered to demonstrate the effectiveness of the proposed approach for multiple-load case situations. The sizes are $L_x = 8$ m and $L_y = 1$ m. Two vertical load cases are applied at the end of the structure. The magnitudes of the two load

cases are assumed to be identical as $F_1 = F_2 = 1.8$ kN but the directions are opposite. The displacements of the DOFs applied by loads are subject to a displacement limit of $[-\bar{U}, \bar{U}]$ where $\bar{U} = \frac{1}{100}L_x$. The service life of the structure is assumed to be 20 years and the average frequency of application of loading is 5 times per hour for both load cases.

The rectangular domain of $L_x \times L_y$ is discretized into 480×60 square elements and a filter radius of $r_{min} = 7.2$ is adopted in the optimization. A small domain with a width of 48 elements at the tip of the structure is set as a passive domain that is occupied by passive material and small bar areas with a width of two elements at the top and bottom surface of the design domain are set as passive domains that should be occupied by solid material. The loadings

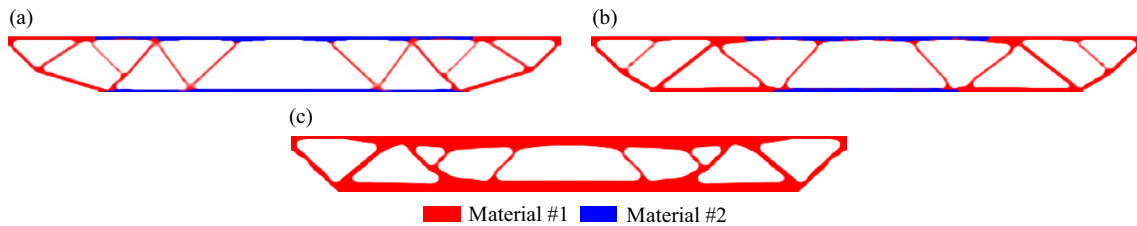


Fig. 13 Optimized designs for carbon minimization of bridge structure: **a** embodied GHG-minimized active structure, **b** total GHG-minimized active structure, and **c** GHG-minimized passive structure

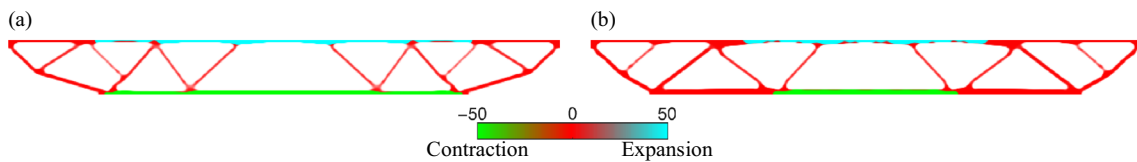
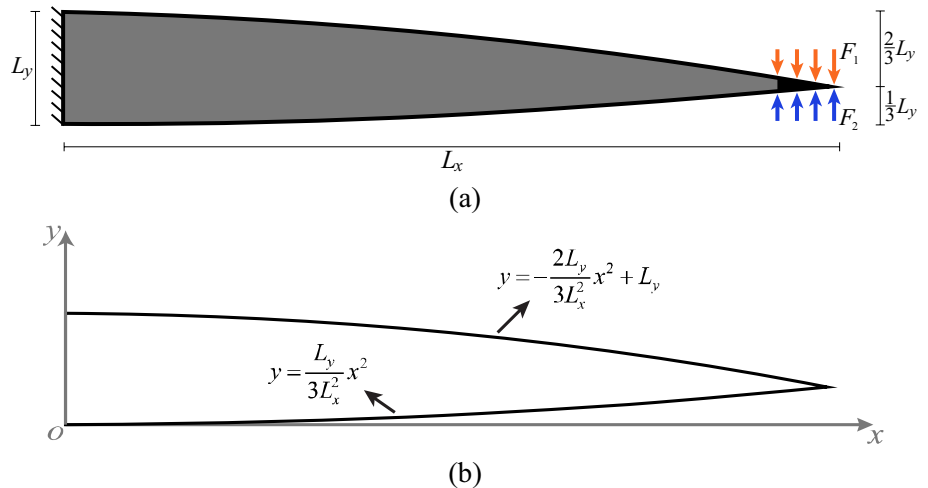


Fig. 14 Actuation effects of active material in optimized active structures: **a** embodied GHG minimization and **b** total GHG minimization

Fig. 15 Design domain of cantilever structure: **a** sizes and **b** geometry description



are evenly applied to the passive domain at the tip of the structure.

4.2.1 Weight minimization

Figure 16 shows the optimized designs of the active structure and corresponding passive structure. As can be seen, both the active and passive structures consist of two materials, but the active structure has much smaller component sizes than the passive structure due to the contribution of the active actuation against the external loading. The weight of the active structure is 7.62 kg composed of 3.73 kg passive material and 3.89 kg active material, while the weight of the passive structure is 12.73 kg, 40.19% heavier than the active structure.

From Table 1, the passive material has a higher modulus-to-density ratio, but it can be seen from Fig. 16b that the passive structure is composed of both passive and active materials. This is because a solution composed of only passive material can not satisfy the displacement constraints, which is verified by the optimization procedure; therefore, a small amount of active material with higher Young's modulus is present in the optimized topology.

The topologies of the active and passive structures are slightly different on the inner components. Note that the geometry and material distributions of the optimized structures are not symmetrical because the design domain is not symmetrical up and down. The active structure has some small crossing components while the passive structure has some small thick vertical components distributed inside. This is because, for the passive structure the stiffness to

external loading is mostly from the two thick top and bottom chords and thus the inner components are not necessary to contribute too much. Figure 17 shows the deformations of the two structures under the two load cases. For the active structure, under both load cases, the displacements caused by the external loading exceed the limits, but the final displacements offset by the actuation are all within the limits. For the passive structure, all the displacements caused by the external loadings are within the displacement limits because the structure can provide sufficient stiffness by itself.

Figure 18 shows the actuation effects of active material in the active design under the two load cases. Unlike the one-load case where the active material has only one actuation effect, the active materials may have different actuation effects under different load cases for multi-load cases. In this example, since the two load cases have opposite effects on the structure, the active materials also have opposite actuation effects under the two load cases.

4.2.2 Energy minimization

Figure 19 shows the optimized active structures obtained through embodied and total energy minimization and the corresponding energy-minimized passive structure. As can be seen, the active structure obtained through embodied energy minimization has smaller component sizes due to a larger amount of active material. Table 2 summarizes the results of embodied, operational, and total energy of the optimized structures. For the two active structures, although the active design obtained through embodied energy minimization has a smaller embodied energy but

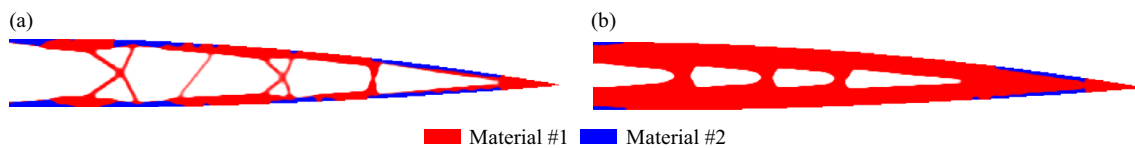


Fig. 16 Optimized designs of active and passive structures of cantilever structure

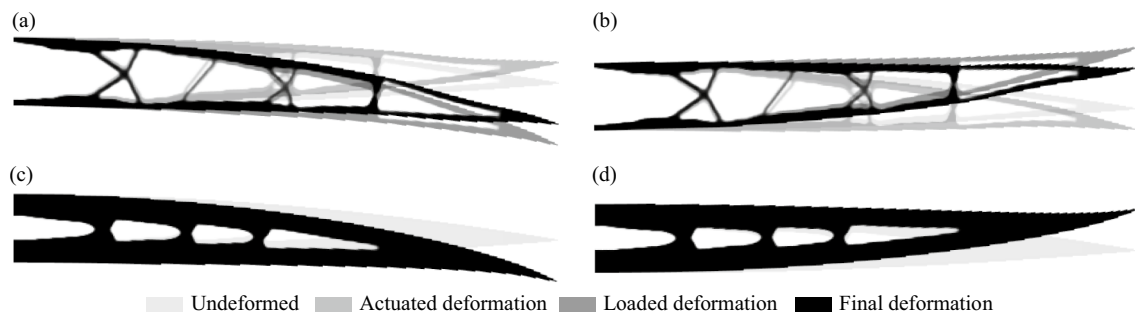


Fig. 17 Deformations of weight-minimized active and structures: **a**, **b** are respectively active structures under first and second load case; **c** and **d** are respectively passive structures under first and second load case

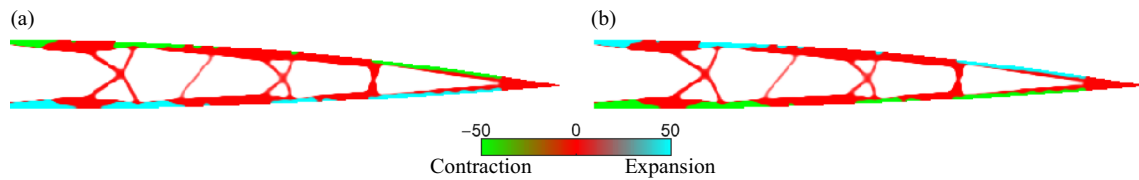


Fig. 18 Actuation effects of active material in weight-minimized active cantilever structure under **a** first and **b** second load case

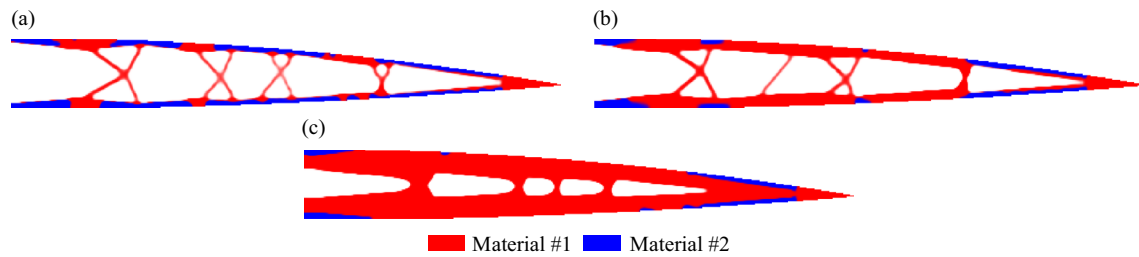


Fig. 19 Optimized designs for energy minimization of cantilever structure: **a** embodied energy-minimized active structure, **b** total energy-minimized active structure, and **c** energy-minimized passive structure

Table 2 Summary information of energy-minimized cantilever structures

	Embodied energy (MJ)	Operational energy (MJ)	Total energy (MJ)
Embodied energy-minimized active design	787.52	303.80	1091.32
Total energy-minimized active design	874.70	135.88	1010.60
Energy-minimized passive design	1480.40	–	1480.40

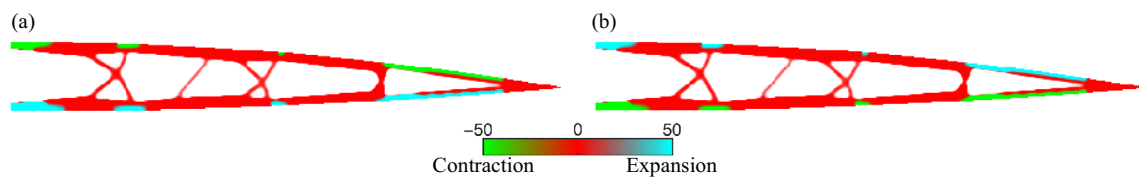


Fig. 20 Actuation effects of active material in total energy-minimized active cantilever structure under **a** first and **b** second load case

results in a larger total energy due to the large share of operational energy cost for the actuation. This further indicates that the operational energy cannot be ignored in the optimal design of active structures in order to reduce energy consumption. On the other hand, Table 2 shows that the two active structures have smaller total energy consumption compared to the optimized passive design, which further reveals that active structures have the potential to save energy compared to passive structures.

Different amounts of materials also result in slightly different topologies of the two active structures, but the actuation effects of the active materials are similar. As an illustration, Fig. 20 shows the actuation effects of the active materials in the total energy-minimized design under different load cases. Similar to the weight-minimized

solutions, the active materials have opposite actuation effects under the two load cases, which ensures the deformations within limits under both load cases.

4.2.3 GHG emission minimization

Figure 21 shows the optimized designs obtained through GHG emission minimization. Table 3 summarizes the results of the solutions. Similar to energy minimization, the active structure obtained through total GHG emission minimization has less active material but larger component sizes than that obtained through embodied GHG emission minimization. Though the active structure obtained through total GHG emission minimization has a larger embodied GHG emission, it achieves a smaller total GHG emission. Again,

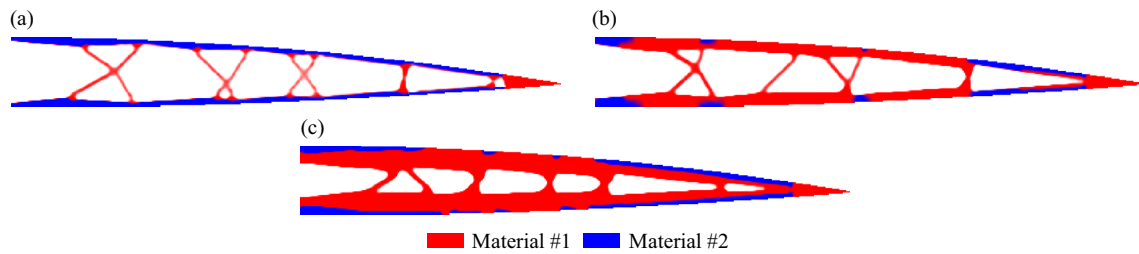


Fig. 21 Optimized designs for carbon minimization of cantilever structure: **a** embodied GHG-minimized active structure, **b** total GHG-minimized active structure, and **c** GHG-minimized passive structure

Table 3 Summary information of carbon-minimized cantilever structures

	Embodied carbon (kgCO ₂ e)	Operational carbon (kgCO ₂ e)	Total carbon (kgCO ₂ e)
Embodied GHG-minimized active design	70.79	65.20	135.99
Total GHG-minimized active design	89.17	20.62	109.79
GHG-minimized passive design	150.55	–	150.55

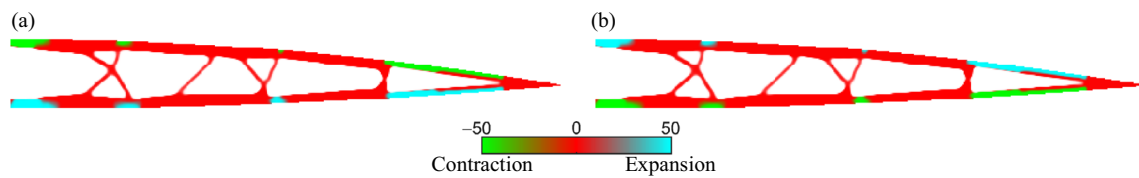


Fig. 22 Actuation effects of active material in total GHG-minimized active cantilever structure under **a** first and **b** second load case

the optimized passive design has larger GHG emissions than both of the two active structures.

The active material distributions and actuation effects are similar to the designs obtained through weight and energy minimization, which are shown in Fig. 22. With the help of actuation, all the displacement limits are respected in the final deformation of the structure.

4.3 Shelter structure

In this example, a shelter structure as shown in Fig. 23 is considered to demonstrate the potential applicability of the proposed approach to the optimal design of multi-material energy-harvesting mechanical structures or devices. The sizes are $L_x = 6$ m and $L_y = 1.8$ m. The middle white part is a void domain that will not be considered in the design. Two evenly-distributed load cases are applied at the top of the structure. The magnitudes of the two distributed load cases are $p_1 = 1.0$ kN/m and $p_2 = 0.3$ kN/m, and their directions are opposite. The displacements of the DOFs applied by loads are subject to a displacement limit of $[-\bar{U}, \bar{U}]$ where $\bar{U} = \frac{1}{500}L_x$. The service life of the structure

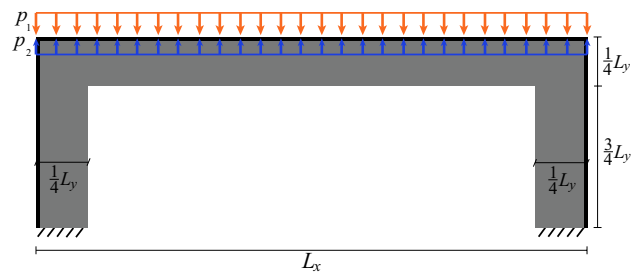


Fig. 23 Design domain and loading of shelter structure

is assumed to be 20 years and the average frequency of application of loading is 5 times per hour for both load cases.

The whole domain of $L_x \times L_y$ is discretized into 300×90 square elements and a filter radius of $r_{\min} = 5$ is adopted in the optimization. A small domain with a width of three elements at the outer surface of the design domain is set as the passive domain that should be occupied by solid material. The distributed loadings are applied to all the nodes at the top of the structure.

Figure 24 shows the optimized designs of active and passive structures obtained through total energy minimization. The active design is made of two materials while the passive design is made of only passive material. The two structures have similar topologies, but the passive structure has larger component sizes. It shows that the active design has a total energy of 508.13 MJ, which is 8% smaller than the passive design.

Figure 25 shows the actuation effects of the active materials under different load cases. As can be seen, the actuation only happens under the first load case. The reason is that the magnitude of the second load case is smaller than the first load case and the deformation caused by the second load is already within the displacement limits (Fig. 26), therefore, to reduce energy consumption, the active material does not need to exert actuation on the structure for the second load case.

Notably, the results above are obtained by only considering energy consumption in the optimization, i.e., the energy harvesting effect is ignored (see Sect. 3.2.4). If the energy harvesting effect is taken into account, different solutions may be obtained. Still, take the case of energy minimization as an example, Fig. 27 shows the configuration of the active structure obtained by considering the energy harvesting effect. As can be seen, the structural topology is similar to that obtained without considering the energy harvesting effect. However, the active material exerts actuation on the structure under the second load case and results in an operational energy of -4.13 MJ instead of zero. This indicates that the actuation in the second load case results in energy harvesting, which can be confirmed by the actuation effects of the active materials (Fig. 27b). The actuation under the second load case has the same effect as the external loading, i.e., they both cause upward deformations of the structure (Fig. 28), which means that the actuation under the

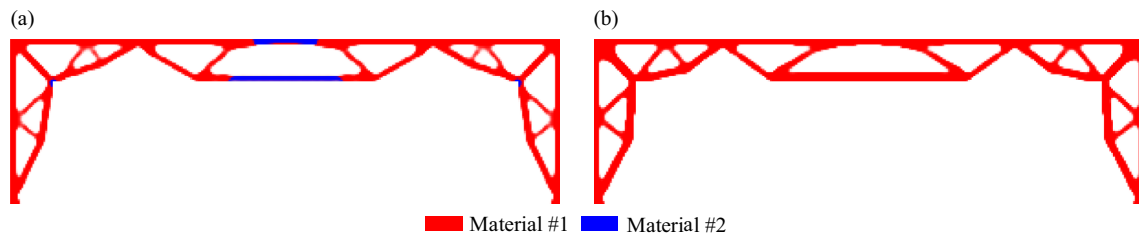


Fig. 24 Optimized designs of shelter structure obtained through total energy minimization: **a** active design and **b** passive design

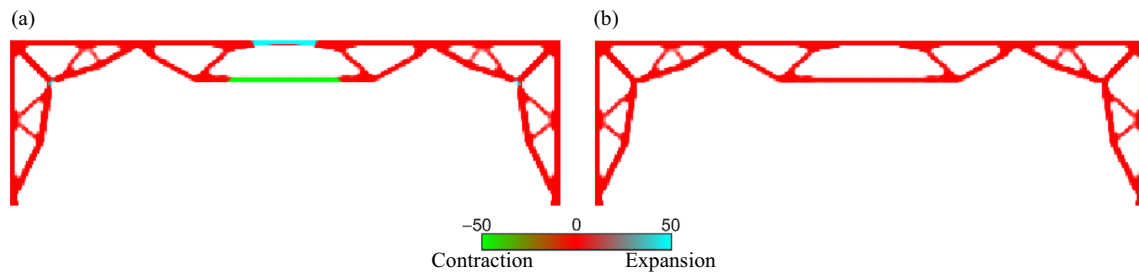


Fig. 25 Actuation effects of active material in total energy-minimized active shelter structure under **a** first and **b** second load case

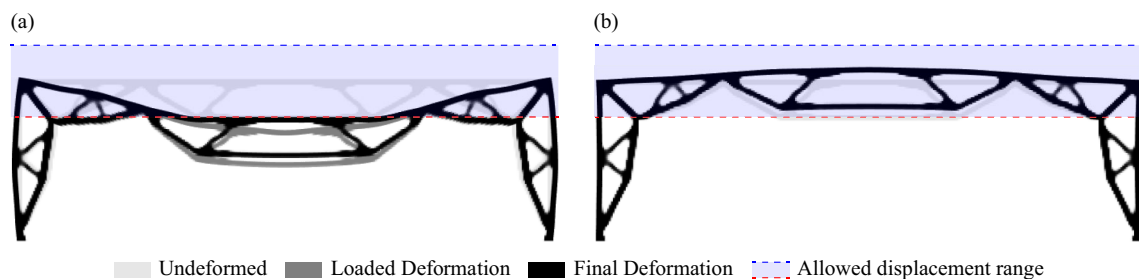


Fig. 26 Deformations of total energy-minimized active shelter structure under **a** first and **b** second load case

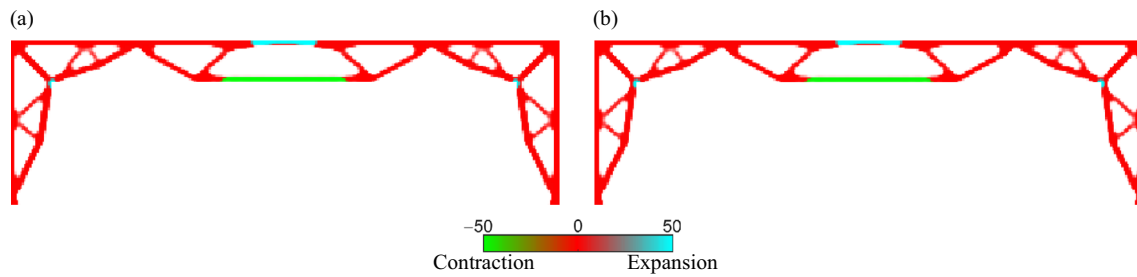


Fig. 27 Actuation effects of active material in total energy-minimized active shelter structure considering energy harvesting: **a** first load case and **b** second load case

second load case could “gain” energy from the deforming process and thus, in turn, resulting in a lower total energy consumption of 503.66 MJ. This example indicates that the proposed approach has the potential to be applied to the optimal design of multi-material energy-harvesting mechanical structures or devices, which could further reduce the environmental impact.

5 Discussion and conclusions

This study proposes a methodology for the TO of multi-material active structures to reduce the environmental impact. The environmental impact, e.g., energy consumption or GHG emissions, of a multi-material active structure is assessed and treated as the objective function to be minimized. Structural displacement limits are enforced as constraints in the optimization. Numerical examples demonstrate that the optimized active designs could achieve considerable weight and energy savings and cause less GHG emissions compared to the corresponding topology optimized passive designs.

By using the proposed material interpolation model, the developed TO framework can be used for the optimal design of multi-material active structures under multiple load cases in which different actuation effects may be needed for

different load cases. By using the K–S aggregation function, multiple local displacement limit constraints can be transformed into a single global constraint, which alleviates the computational burden during the optimization. In addition, the proposed framework has been used to apply to the optimal design of multi-material energy-harvesting mechanical structures or devices.

Many factors affect the environmental impact caused by an active structure, such as material type, structure service life, loading condition and action frequency during the service life, as well as material production process. For an arbitrary design scenario, it is hard to predict whether the optimized active design can outperform the corresponding passive design. By using the proposed approach, the optimizer can automatically choose the better solution with less environmental impact.

Only displacement limits, i.e., structural stiffness constraints, are considered in the current study. Although previous studies have demonstrated that active structures are preferred for stiffness-governed cases regarding weight and energy savings, other important requirements like strength and stability (Wang and Sigmund 2023), should also be considered in practical design. This will be the extension of the study in future work. Finally, we remark that although only 2D plane stress is considered in the examples, the proposed formulations also apply to 3D and plane strain problems.

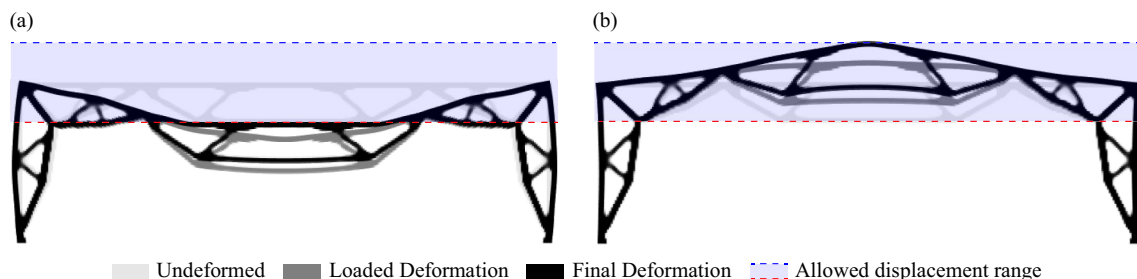


Fig. 28 Deformations of total energy-minimized active shelter structure considering energy harvesting: **a** first load case and **b** second load case

Appendix 1

For an active structure under external loading and actuation, the conversion between different energies follows the following relation

$$E_{load} + E_{operational} = E_{strain} \tag{37}$$

where E_{load} and $E_{operational}$ are the work done by the external loading and active actuation respectively and E_{strain} is the strain energy stored in the materials. Then the work done (i.e., the operational energy consumption) by the actuation can be obtained as

$$E_{operational} = E_{strain} - E_{load} \tag{38}$$

Following assumption #1, the work done by the external loading is given by

$$E_{load} = \frac{1}{2} \mathbf{P}_m^T \mathbf{U}_m + \mathbf{P}_m^T \mathbf{U}_t \tag{39}$$

The material strain energy of a structure under thermo-mechanical loading is given by

$$\begin{aligned} E_{strain} &= \frac{1}{2} \int_V (\boldsymbol{\varepsilon} - \boldsymbol{\varepsilon}_t)^T \mathbf{D} (\boldsymbol{\varepsilon} - \boldsymbol{\varepsilon}_t) dV \\ &= \frac{1}{2} \mathbf{U}^T (\mathbf{P}_m - \mathbf{P}_t) + \frac{1}{2} \int_V (\boldsymbol{\varepsilon}_t)^T \mathbf{D} \boldsymbol{\varepsilon}_t dV \end{aligned} \tag{40}$$

where $\boldsymbol{\varepsilon}$ and $\boldsymbol{\varepsilon}_t$ are the total and thermal strains respectively. Then, from Eq. (38) the work done (i.e., the operational energy consumption) by the actuation can be obtained as

$$\begin{aligned} E_{operational} &= \frac{1}{2} \mathbf{U}^T (\mathbf{P}_m - \mathbf{P}_t) + \frac{1}{2} \int_V (\boldsymbol{\varepsilon}_t)^T \mathbf{D} \boldsymbol{\varepsilon}_t dV - \left(\frac{1}{2} \mathbf{U}_m^T \mathbf{P}_m + \mathbf{U}_m^T \mathbf{P}_t \right) \\ &= -\left(\mathbf{U}_m + \frac{1}{2} \mathbf{U}_t \right)^T \mathbf{P}_t + \frac{1}{2} \int_V (\boldsymbol{\varepsilon}_t)^T \mathbf{D} \boldsymbol{\varepsilon}_t dV \end{aligned} \tag{41}$$

Equation (41) coincides with Eq. (34), which further verifies the formulations for the computation of operational energy.

Appendix 2

Sensitivity of Material Mass

The sensitivity of masses of different materials with respect to variables $\tilde{\xi}_e$ and $\tilde{\eta}_e$ can be calculated through Eq. (15) as

$$\begin{aligned} \frac{\partial M_a}{\partial \tilde{\xi}_e} &= \rho_a V_e \tilde{\eta}_e, \quad \frac{\partial M_a}{\partial \tilde{\eta}_e} = \rho_a V_e \tilde{\xi}_e, \\ \frac{\partial M_p}{\partial \tilde{\xi}_e} &= \rho_p V_e (1 - \tilde{\eta}_e), \quad \frac{\partial M_p}{\partial \tilde{\eta}_e} = -\rho_p V_e \tilde{\xi}_e \end{aligned} \tag{42}$$

Note that the material masses are independent of variable χ_e , hence the sensitivities with respect to χ_e are zero.

Sensitivity of Displacement Constraint

Take the first K–S function in Eq. (21) as an example and use \tilde{x}_e to denote the physical-field variables in the following to illustrate the sensitivity analysis of displacement constraints. The sensitivity of the K–S function is given by

$$\frac{\partial J^{KS}(u_i/u_i)}{\partial \tilde{x}_e} = \frac{\sum_{i \in \Theta} e^{q(u_i/u_i - u_i - u_i/u_i)} \frac{\partial (u_i/u_i)}{\partial \tilde{x}_e}}{\sum_{i \in \Theta} e^{q(u_i/u_i - u_i - u_i/u_i)}} = \frac{\sum_{i \in \Theta} e^{q(u_i/u_i - u_i - u_i/u_i)} \frac{1}{u_i} \frac{\partial u_i}{\partial \tilde{x}_e}}{\sum_{i \in \Theta} e^{q(u_i/u_i - u_i - u_i/u_i)}} \tag{43}$$

Define vector \mathbf{Q}_i to convert global displacement vector \mathbf{U} to local displacement u_i , i.e., $u_i = \mathbf{Q}_i \mathbf{U}$ for each nodal displacement with an enforced limit, then

$$\frac{\partial u_i}{\partial \tilde{x}_e} = \mathbf{Q}_i \frac{\partial \mathbf{U}}{\partial \tilde{x}_e} \tag{44}$$

Differentiate both sides of Eq. (12) with respect to \tilde{x}_e gives

$$\frac{\partial \mathbf{K}}{\partial \tilde{x}_e} \mathbf{U} + \mathbf{K} \frac{\partial \mathbf{U}}{\partial \tilde{x}_e} = \frac{\partial \mathbf{P}}{\partial \tilde{x}_e} \tag{45}$$

Considering that $\mathbf{P} = \mathbf{P}_m + \mathbf{P}_t$ and $\frac{\partial \mathbf{P}_m}{\partial \tilde{x}_e} = \mathbf{0}$, $\frac{\partial \mathbf{U}}{\partial \tilde{x}_e}$ is given by

$$\frac{\partial \mathbf{U}}{\partial \tilde{x}_e} = \mathbf{K}^{-1} \left(\frac{\partial \mathbf{P}_t}{\partial \tilde{x}_e} - \frac{\partial \mathbf{K}}{\partial \tilde{x}_e} \mathbf{U} \right) \tag{46}$$

Substituting Eqs. (46) and (44) into Eq. (43) yields

$$\frac{\partial J^{KS}(u_i/u_i)}{\partial \tilde{x}_e} = \frac{\sum_{i \in \Theta} e^{q(u_i/u_i - u_i - u_i/u_i)} \mathbf{Q}_i / u_i}{\sum_{i \in \Theta} e^{q(u_i/u_i - u_i - u_i/u_i)}} \mathbf{K}^{-1} \left(\frac{\partial \mathbf{P}_t}{\partial \tilde{x}_e} - \frac{\partial \mathbf{K}}{\partial \tilde{x}_e} \mathbf{U} \right) \tag{47}$$

Let $\boldsymbol{\lambda}^T = \frac{\sum_{i \in \Theta} e^{q(u_i/u_i - u_i - u_i/u_i)} \mathbf{Q}_i / u_i}{\sum_{i \in \Theta} e^{q(u_i/u_i - u_i - u_i/u_i)}} \mathbf{K}^{-1}$, i.e.,

$\mathbf{K} \boldsymbol{\lambda} = \frac{\sum_{i \in \Theta} e^{q(u_i/u_i - u_i - u_i/u_i)} \mathbf{Q}_i / u_i}{\sum_{i \in \Theta} e^{q(u_i/u_i - u_i - u_i/u_i)}}$, then the sensitivity is given by

$$\frac{\partial J^{KS}(u_i/u_i)}{\partial \tilde{x}_e} = \boldsymbol{\lambda}^T \left(\frac{\partial \mathbf{P}_t}{\partial \tilde{x}_e} - \frac{\partial \mathbf{K}}{\partial \tilde{x}_e} \mathbf{U} \right) \tag{48}$$

where $\frac{\partial \mathbf{K}}{\partial \tilde{x}_e}$ and $\frac{\partial \mathbf{P}_t}{\partial \tilde{x}_e}$ are given by

$$\begin{aligned}\frac{\partial \mathbf{K}}{\partial \tilde{x}_e} &= \frac{\partial h_e}{\partial \tilde{x}_e} \int_{V_e} \mathbf{B}_e^T \mathbf{D}_0 \mathbf{B}_e dV \\ \frac{\partial \mathbf{P}_t}{\partial \tilde{x}_e} &= \frac{\partial h_e}{\partial \tilde{x}_e} \int_{V_e} \mathbf{B}_e^T \mathbf{D}_0 \boldsymbol{\varepsilon}_{\Delta T, e} dV + \frac{\partial \alpha_e}{\partial \tilde{x}_e} \int_{V_e} \mathbf{B}_e^T \mathbf{D}_e \boldsymbol{\Phi}^T \Delta T_e dV \\ &\quad + \frac{\partial \Delta T_e}{\partial \tilde{x}_e} \int_{V_e} \mathbf{B}_e^T \mathbf{D}_e \boldsymbol{\Phi}^T \alpha_e dV\end{aligned}\quad (49)$$

where $\frac{\partial h_e}{\partial \tilde{x}_e}$, $\frac{\partial \alpha_e}{\partial \tilde{x}_e}$, and $\frac{\partial \Delta T_e}{\partial \tilde{x}_e}$ can be calculated through Eqs. (11), (9), and (16), respectively.

Sensitivity of Operational Energy

From Eq. (34), the sensitivity of operational energy with respect to \tilde{x}_e is given by

$$\begin{aligned}\frac{\partial E_{\text{operational}}}{\partial \tilde{x}_e} &= -\frac{\partial \left(\mathbf{U}_m + \frac{1}{2} \mathbf{U}_t \right)^T}{\partial \tilde{x}_e} \mathbf{P}_t - \left(\mathbf{U}_m + \frac{1}{2} \mathbf{U}_t \right)^T \frac{\partial \mathbf{P}_t}{\partial \tilde{x}_e} \\ &\quad + \int_{V_e} \mathbf{D}_e \boldsymbol{\varepsilon}_{\Delta T, e} \frac{\partial \boldsymbol{\varepsilon}_{\Delta T, e}}{\partial \tilde{x}_e} dV \\ &\quad + \frac{1}{2} \int_{V_e} \left(\boldsymbol{\varepsilon}_{\Delta T, e} \right)^T \mathbf{D}_0 \boldsymbol{\varepsilon}_{\Delta T, e} \frac{\partial h_e}{\partial \tilde{x}_e} dV\end{aligned}\quad (50)$$

The first term on the right side of Eq. (50) can be rewritten as

$$\begin{aligned}-\frac{\partial \left(\mathbf{U}_m + \frac{1}{2} \mathbf{U}_t \right)^T}{\partial \tilde{x}_e} \mathbf{P}_t &= -\mathbf{P}_t^T \frac{\partial \mathbf{U}_m}{\partial \tilde{x}_e} - \frac{1}{2} \mathbf{P}_t^T \frac{\partial \mathbf{U}_t}{\partial \tilde{x}_e} \\ &= -\mathbf{P}_t^T \mathbf{K}^{-1} \left(-\frac{\partial \mathbf{K}}{\partial \tilde{x}_e} \mathbf{U}_m \right) - \frac{1}{2} \mathbf{P}_t^T \mathbf{K}^{-1} \left(\frac{\partial \mathbf{P}_t}{\partial \tilde{x}_e} - \frac{\partial \mathbf{K}}{\partial \tilde{x}_e} \mathbf{U}_p \right)\end{aligned}\quad (51)$$

Let $\boldsymbol{\lambda}_1^T = -\mathbf{P}_t^T \mathbf{K}^{-1}$ and $\boldsymbol{\lambda}_2^T = -\frac{1}{2} \mathbf{P}_t^T \mathbf{K}^{-1}$, i.e., $\boldsymbol{\lambda}_1 = -\mathbf{U}_t$ and $\boldsymbol{\lambda}_2 = -\frac{1}{2} \mathbf{U}_t$, then Eq. (51) can be simplified as

$$-\frac{\partial \left(\mathbf{U}_m + \frac{1}{2} \mathbf{U}_t \right)^T}{\partial \tilde{x}_e} \mathbf{P}_t = -\mathbf{U}_t^T \left(-\frac{\partial \mathbf{K}}{\partial \tilde{x}_e} \mathbf{U}_m \right) - \frac{1}{2} \mathbf{U}_t^T \left(\frac{\partial \mathbf{P}_t}{\partial \tilde{x}_e} - \frac{\partial \mathbf{K}}{\partial \tilde{x}_e} \mathbf{U}_p \right)\quad (52)$$

The second term on the right side of Eq. (50) can be calculated by using Eq. (49). $\frac{\partial \boldsymbol{\varepsilon}_{\Delta T, e}}{\partial \tilde{x}_e}$ in the third term is given by

$$\frac{\partial \boldsymbol{\varepsilon}_{\Delta T, e}}{\partial \tilde{x}_e} = \frac{\partial \alpha_e}{\partial \tilde{x}_e} \boldsymbol{\Phi}^T \Delta T_e + \alpha_e \boldsymbol{\Phi}^T \frac{\partial \Delta T_e}{\partial \tilde{x}_e}\quad (53)$$

Based on the analysis and formulations derived above, the sensitivities of the objective function and constraints can be calculated accordingly.

Acknowledgements Yafeng Wang is supported by the European Union's Horizon 2020 research and innovation programme under the Marie Skłodowska-Curie Fellowship (Grant No. 899987). Ole Sigmund is supported by the Villum Foundation through the Villum Investigator Project InnoTop.

Funding Open access funding provided by Technical University of Denmark.

Declarations

Conflict of interest The authors declare that they have no known competing financial interests or personal relationships that could have appeared to influence the work reported in this paper.

Replication of results The numerical results presented in this document can be replicated using the methodology and formulations described herein. The data used in the examples are available upon request to the corresponding author.

Open Access This article is licensed under a Creative Commons Attribution 4.0 International License, which permits use, sharing, adaptation, distribution and reproduction in any medium or format, as long as you give appropriate credit to the original author(s) and the source, provide a link to the Creative Commons licence, and indicate if changes were made. The images or other third party material in this article are included in the article's Creative Commons licence, unless indicated otherwise in a credit line to the material. If material is not included in the article's Creative Commons licence and your intended use is not permitted by statutory regulation or exceeds the permitted use, you will need to obtain permission directly from the copyright holder. To view a copy of this licence, visit <http://creativecommons.org/licenses/by/4.0/>.

References

- Allaire G, Jouve F, Toader A-M (2004) Structural optimization using sensitivity analysis and a level-set method. *J Comput Phys* 194:363–393. <https://doi.org/10.1016/j.jcp.2003.09.032>
- Bendsøe MP, Kikuchi N (1988) Generating optimal topologies in structural design using a homogenization method. *Comput Methods Appl Mech Eng* 71:197–224. [https://doi.org/10.1016/0045-7825\(88\)90086-2](https://doi.org/10.1016/0045-7825(88)90086-2)
- Bendsøe MP, Sigmund O (2003) *Topology optimization: Theory, Methods, and Applications*. Springer, Berlin
- Cabeza LF, Boquera L, Chàfer M, Vézé D (2021) Embodied energy and embodied carbon of structural building materials: Worldwide progress and barriers through literature map analysis. *Energy Build* 231:110612. <https://doi.org/10.1016/j.enbuild.2020.110612>
- Chandrasekhar A, Suresh K (2021) Multi-material topology optimization using neural networks. *Comput Aided Des* 136:103017. <https://doi.org/10.1016/j.cad.2021.103017>
- Ching E, Carstensen JV (2022) Truss topology optimization of timber–steel structures for reduced embodied carbon design. *Eng Struct* 252:113540. <https://doi.org/10.1016/j.engstruct.2021.113540>
- Chu S, Xiao M, Gao L, Li H, Zhang J, Zhang X (2019) Topology optimization of multi-material structures with graded interfaces. *Comput Methods Appl Mech Eng* 346:1096–1117. <https://doi.org/10.1016/j.cma.2018.09.040>
- De Leon DM, Alexandersen J, Fonseca JSO, Sigmund O (2015) Stress-constrained topology optimization for compliant mechanism

- design. *Struct Multidisc Optim* 52:929–943. <https://doi.org/10.1007/s00158-015-1279-z>
- Gangl P (2020) A multi-material topology optimization algorithm based on the topological derivative. *Comput Methods Appl Mech Eng* 366:113090. <https://doi.org/10.1016/j.cma.2020.113090>
- Gao T, Zhang W (2011) A mass constraint formulation for structural topology optimization with multiphase materials. *Int J Numer Meth Eng* 88:774–796. <https://doi.org/10.1002/nme.3197>
- Gibiansky LV, Sigmund O (2000) Multiphase composites with extremal bulk modulus. *J Mech Phys Solids* 48:461–498. [https://doi.org/10.1016/S0022-5096\(99\)00043-5](https://doi.org/10.1016/S0022-5096(99)00043-5)
- Gossweiler GR, Brown CL, Hewage GB, Sapiro-Gheiler E, Trautman WJ, Welshofer GW, Craig SL (2015) Mechanochemically active soft robots. *ACS Appl Mater Interfaces* 7:22431–22435. <https://doi.org/10.1021/acsami.5b06440>
- Huang X, Xie M (2010) Evolutionary topology optimization of continuum structures: methods and applications. Wiley, Chichester
- Huang X, Xie YM, Jia B, Li Q, Zhou SW (2012) Evolutionary topology optimization of periodic composites for extremal magnetic permeability and electrical permittivity. *Struct Multidisc Optim* 46:385–398. <https://doi.org/10.1007/s00158-012-0766-8>
- Jensen PDL, Wang F, Dimino I, Sigmund O (2021) Topology optimization of large-scale 3D morphing wing structures. *Actuators* 10:217. <https://doi.org/10.3390/act10090217>
- Kreisselmeier G, Steinhauser R (1980) Systematic control design by optimizing a vector performance index. In: Computer aided design of control systems. Elsevier, Maryland Heights, pp 113–117
- Le C, Norato J, Bruns T, Ha C, Tortorelli D (2010) Stress-based topology optimization for continua. *Struct Multidisc Optim* 41:605–620. <https://doi.org/10.1007/s00158-009-0440-y>
- Li D, Kim IY (2018) Multi-material topology optimization for practical lightweight design. *Struct Multidisc Optim* 58:1081–1094. <https://doi.org/10.1007/s00158-018-1953-z>
- Liu P, Luo Y, Kang Z (2016) Multi-material topology optimization considering interface behavior via XFEM and level set method. *Comput Methods Appl Mech Eng* 308:113–133. <https://doi.org/10.1016/j.cma.2016.05.016>
- Liu P, Shi L, Kang Z (2020) Multi-material structural topology optimization considering material interfacial stress constraints. *Comput Methods Appl Mech Eng* 363:112887. <https://doi.org/10.1016/j.cma.2020.112887>
- Long K, Wang X, Gu X (2018) Multi-material topology optimization for the transient heat conduction problem using a sequential quadratic programming algorithm. *Eng Optim* 50:2091–2107. <https://doi.org/10.1080/0305215X.2017.1417401>
- Luo Y, Li Q, Liu S (2019) Topology optimization of shell–infill structures using an erosion-based interface identification method. *Comput Methods Appl Mech Eng* 355:94–112. <https://doi.org/10.1016/j.cma.2019.05.017>
- Mirzendehtel AM, Suresh K (2015) A Pareto-optimal approach to multimaterial topology optimization. *J Mech Des* 137:101701. <https://doi.org/10.1115/1.4031088>
- Preumont A (2018) Vibration control of active structures: an introduction. Springer, Berlin
- Qader İN, Mediha K, Dagdelen F, Aydođdu Y (2019) A review of smart materials: researches and applications. *El-Cezeri* 6:755–788
- Reksowardojo AP, Senatore G, Srivastava A, Carroll C, Smith IFC (2022) Design and testing of a low-energy and-carbon prototype structure that adapts to loading through shape morphing. *Int J Solids Struct* 252:111629. <https://doi.org/10.1016/j.ijsolstr.2022.111629>
- Senatore G, Duffour P, Winslow P (2019) Synthesis of minimum energy adaptive structures. *Struct Multidisc Optim*. <https://doi.org/10.1007/s00158-019-02224-8>
- Sigmund O (2001a) Design of multiphysics actuators using topology optimization—part II: two-material structures. *Comput Methods Appl Mech Eng* 190:6605–6627. [https://doi.org/10.1016/S0045-7825\(01\)00252-3](https://doi.org/10.1016/S0045-7825(01)00252-3)
- Sigmund O (2001b) Design of multiphysics actuators using topology optimization—part I: one-material structures. *Comput Methods Appl Mech Eng* 190:6577–6604. [https://doi.org/10.1016/S0045-7825\(01\)00251-1](https://doi.org/10.1016/S0045-7825(01)00251-1)
- Sigmund O, Torquato S (1997) Design of materials with extreme thermal expansion using a three-phase topology optimization method. *J Mech Phys Solids* 45:1037–1067. [https://doi.org/10.1016/S0022-5096\(96\)00114-7](https://doi.org/10.1016/S0022-5096(96)00114-7)
- Sofla A, Meguid S, Tan K, Yeo W (2010) Shape morphing of aircraft wing: status and challenges. *Mater Des* 31:1284–1292. <https://doi.org/10.1016/j.matdes.2009.09.011>
- Stegmann J, Lund E (2005) Discrete material optimization of general composite shell structures. *Int J Numer Methods Eng* 62:2009–2027. <https://doi.org/10.1002/nme.1259>
- Sun S, Zhang W (2006) Multiple objective topology optimal design of multiphase microstructures. *Acta Mech Sin Chin Ed* 38:633
- Svanberg K (1987) The method of moving asymptotes—a new method for structural optimization. *Int J Numer Methods Eng* 24:359–373. <https://doi.org/10.1002/nme.1620240207>
- Thomsen J (1992) Topology optimization of structures composed of one or two materials. *Struct Optim* 5:108–115. <https://doi.org/10.1007/BF01744703>
- Wang Y, Senatore G (2020) Minimum energy adaptive structures—All-In-One problem formulation. *Comput Struct* 236:106266. <https://doi.org/10.1016/j.compstruc.2020.106266>
- Wang Y, Senatore G (2021) Design of adaptive structures through energy minimization: extension to tensegrity. *Struct Multidisc Optim* 64:1079–1110
- Wang Y, Sigmund O (2023) Multi-material topology optimization for maximizing structural stability under thermo-mechanical loading. *Comput Methods Appl Mech Eng* 407:115938. <https://doi.org/10.1016/j.cma.2023.115938>
- Wang MY, Wang X (2004) “Color” level sets: a multi-phase method for structural topology optimization with multiple materials. *Comput Methods Appl Mech Eng* 193:469–496. <https://doi.org/10.1016/j.cma.2003.10.008>
- Wang F, Lazarov BS, Sigmund O (2011) On projection methods, convergence and robust formulations in topology optimization. *Struct Multidisc Optim* 43:767–784. <https://doi.org/10.1007/s00158-010-0602-y>
- Wang Y, Luo Z, Zhang X, Kang Z (2014) Topological design of compliant smart structures with embedded movable actuators. *Smart Mater Struct* 23:045024. <https://doi.org/10.1088/0964-1726/23/4/045024>
- Wang Y, Xu X, Luo Y (2021) Minimal mass design of active tensegrity structures. *Eng Struct* 234:111965. <https://doi.org/10.1016/j.engstruct.2021.111965>
- Wang Y, Luo Y, Yan Y (2022) A multi-material topology optimization method based on the material-field series-expansion model. *Struct Multidisc Optim* 65:1–15
- Wein F, Dunning PD, Norato JA (2020) A review on feature-mapping methods for structural optimization. *Struct Multidisc Optim* 62:1597–1638
- Xu S, Liu J, Zou B, Li Q, Ma Y (2021) Stress constrained multi-material topology optimization with the ordered SIMP method. *Comput Methods Appl Mech Eng* 373:113453. <https://doi.org/10.1016/j.cma.2020.113453>
- Xu X, You J, Wang Y, Luo Y (2023) Analysis and assessment of life-cycle carbon emissions of space frame structures. *J Clean Prod* 385:135521. <https://doi.org/10.1016/j.jclepro.2022.135521>
- Ye H-L, Dai Z-J, Wang W-W, Sui Y-K (2019) ICM method for topology optimization of multimaterial continuum structure with

displacement constraint. *Acta Mech Sin* 35:552–562. <https://doi.org/10.1007/s10409-018-0827-3>

You J, Xu X, Wang Y, Xiang X, Luo Y (2023) Life cycle carbon emission assessment of large-span steel structures: a case study. *Structures* 52:842–853

Publisher's Note Springer Nature remains neutral with regard to jurisdictional claims in published maps and institutional affiliations.